

XMM-NEWTON EPIC BACKGROUND MODELING FOR EXTENDED SOURCES

J. NEVALAINEN^{1,2}, M. MARKEVITCH^{1,4}, D. LUMB³
Harvard-Smithsonian Center for Astrophysics, Cambridge, USA¹
Observatory, University of Helsinki, Finland²
ESTEC, Noordwijk, Netherlands³
IKI, Moscow, Russia⁴
Accepted for publication in ApJ

ABSTRACT

We use XMM-Newton blank-sky and closed-cover background data to explore the background subtraction methods for large extended sources filling the EPIC field of view, such as nearby galaxy clusters, for which local background estimation is difficult. In particular, we investigate the uncertainties of the background modeling in the 0.8–7.0 keV band that affect the cluster analyses. To model the background, we have constructed composite datasets from the blank-sky observations and compared them to the individual blank-sky observations to evaluate the modeling error. Our results apply to data obtained with thin and medium optical filters and in Full frame and Extended full frame modes.

As expected, the modeling uncertainty is determined by how the EPIC background flares are filtered. We find that to keep this uncertainty tolerable, one has to use a much more restrictive filter than that commonly applied. In particular, because flares have highly variable spectra, not all of them are identified by filtering the $E > 10$ keV light curve. We tried using the outer part of the EPIC FOV for monitoring the background in a softer band (1–5 keV). We find that one needs to discard the time periods when either the hard-band or the soft-band rate exceeds the nominal value by more than 20% in order to limit the 90% CL background uncertainty to between $\pm 5\%$ at $E = 4–7$ keV and $\pm 20\%$ at $E = 0.8–1$ keV, for both MOS and PN. This compares to a 10–30% respective PN uncertainty when only the hard-band light curve is used for filtering, and to a 15–45% PN uncertainty when applying the commonly used $2–3\sigma$ filtering method. Adding such a soft-band filter on average results in only a 5–10% reduction of the useful exposure time.

We illustrate our method on a nearby cluster A1795. The above background uncertainties convert into the systematic temperature uncertainties between $\sim \pm 1\%$ at $r = 3–4'$ and $\pm 20–25\%$ ($\sim \pm 1$ keV for A1795) at $r = 10–15'$. For comparison, the commonly applied $2–3\sigma$ clipping of the hard-band light curve misses a significant amount of flares, rendering the temperatures beyond $r = 10'$ unconstrained. Thus, the background uncertainties do not prohibit the EPIC temperature profile analysis of low-brightness regions, like outer regions of galaxy clusters, provided a conservative flare filtering such as the double filtering method with $\pm 20\%$ limits is used.

Subject headings: galaxies: clusters: general — galaxies: clusters: individual (Abell 1795) — X-rays: galaxies

1. INTRODUCTION

The total background emission in XMM-Newton EPIC instruments is known to have a time-variable (i.e., flaring) component, in addition to the sky background (Cosmic X-ray background + the Galactic emission) and a relatively quiescent cosmic ray induced internal background components. The first-order remedy is to filter the data using a high energy light curve, where the particle background dominates the emission (e.g., Arnaud et al. 2001; Lumb et al. 2002). The hard band filtering may miss flares that are more variable at lower energies. When the outer parts of the FOV can be used for direct local background estimation, the effects of any remaining flares can be minimized (e.g. Zhang et al., 2004). However, the background estimation is more complicated for such extended sources, like nearby bright clusters of galaxies, which fill the whole FOV and thus do not allow unambiguous local background estimate to be obtained. In this case one has to use a blank sky based background estimate (see Lumb et al. 2002; Read & Ponman 2003). As of January 2005, XMM-Newton has observed or is scheduled to observe ~ 80 nearby ($z < 0.1$) clusters of galaxies, for which the blank sky subtraction has to be used.

The uncertainties involved in the blank sky based background estimation may have a significant effect on the temper-

ature measurements of low-brightness sources like the outer parts of clusters of galaxies. However, these effects have not been systematically evaluated in the works on the XMM-Newton background published to date (e.g., Lumb et al. 2002; Marty et al. 2003, Read & Ponman 2003). Consequently, the uncertainties have not been properly propagated to most XMM-Newton cluster temperature measurements that used blank sky backgrounds.

Our goals in this paper are to evaluate these uncertainties by comparing a quiescent background spectrum prediction with a sample of XMM-Newton EPIC blank sky data, and to explore ways to minimize these uncertainties. We compare different methods of flare filtering and normalizing the blank sky background spectrum for a given observation. We expand the background analysis work of Katayama et al. (2004), e.g. by studying the MOS data and including more PN data and mild PN flares into the analysis.

We describe a recipe for propagating the uncertainties of the quiescent background predictions to the cluster temperature measurements. We illustrate this recipe by performing spatially resolved spectroscopy of a bright nearby cluster A1795, whose XMM observations are strongly affected by flares.

2. ANALYSIS

We processed the raw data with the SAS 5.4.1 tools `epchain` and `emchain`, with the latest calibration constituents available in Jan 2004. We selected events with patterns 0-4 (single + double) and 0-12 for PN and MOS, respectively. We used `evselect` tool to extract spectra, images and light curves, and the `arfgen` tool to generate auxiliary response files. In the spectral fits we used the latest ready-made on-axis energy redistribution files. We further filtered the data with SAS expression “`flag==0`” to exclude bad pixels and CCD gaps, and excluded the regions of bright point sources. When analyzing the hard band light curves or images, we select events above energies 10 keV (PN) or 9.5 keV (MOS), up to the instrument’s internal upper limit, but when examining the hard band spectra, we limit the analysis to energy bands 10–14 keV (PN) or 9.5–12 keV (MOS).

At the time of this writing, there is no functional standard tool for performing the exposure correction for the light curve in the SAS distribution, i.e. to correct the light curves for losses in flux due to a number of causes, e.g. ‘true’ dead time, during which events are not recorded at all (see the SAS Packages description in the XMM-Newton web page <http://xmm.vilspa.esa.es>). Thus, in order to obtain generally applicable results, we ignore this correction. Note that our reported count rates and exposure times based on the light curves differ by $\sim 10\%$ from those derived using the spectra, which incorporate exposure correction.

We examined the PN and MOS hard band images for anomalously bright CCDs, without finding any. The exposure times for individual CCDs in a given pointing in closed-cover and blank-sky samples vary by less than 1%. The useful detector area of the full FOV (a circle with a radius of $15'$, centered at (DETX,DETY) = (-2120,-1080) for PN, (0,0) for MOS), after exclusion of CCD gaps, bad pixels, inactive detector regions and point sources varies from observation to observation by only 0.1% for each instrument, with the average values of 615 (PN) and 656 (MOS) arcmin⁻². These values can be used to scale our full FOV count rates, if one excludes a significant fraction of the FOV from the analysis.

3. CLOSED-COVER BACKGROUND

In order to estimate the spectrum of the quiescent particle-induced background, we formed a sample of EPIC data obtained with the filter wheel in closed position (i.e., when no photons from the mirror enter the detectors), see Table 1. The sample consists of all the publicly available closed-filter Full frame or Extended full frame data sets as of Oct 2003, with livetime for the central CCD larger than 5ks in any of the detectors, as reported in the observation log browser in the XMM-Newton web page. We excluded sets which have reported problems of high radiation. In some observations there are periods of high radiation in the beginning and end of the exposure, and we excluded those periods when extracting spectra. Using the hard band (> 10 keV for PN and > 9.5 keV for MOS) light curves of the full FOV closed-cover data in each individual observation, we obtain count rates which are scattered around the sample averages of 0.63 (PN), 0.17 (MOS1) and 0.18 (MOS2) cts s⁻¹ with a standard deviation of 6%.

We formed the average closed-cover spectra by co-adding the individual spectra. The exposure times for the combined spectra are 110 ks, 40 ks, 170 ks and 220 ks for PN Full frame, PN Extended full frame, MOS1 and MOS2, respectively. In

TABLE 1
CLOSED-COVER SAMPLE

obs. ID	exp. ID			obs. start year-mm-dd	exp. time (ks)		
	PN	MOS1	MOS2		PN	MOS1	MOS2
FF							
0086360901	-	S005	S006	2001-03-11	-	10	10
0094170301	-	S001	S002	2001-04-12	-	8	8
0094800301	-	S001	S002	2001-06-21	-	10	10
0108860601	S005	S003	S004	2001-10-14	6	9	9
0109490701	S005	S003	S004	2001-09-07	4	7	7
0111971501	S005	S003	S004	2002-06-01	5	7	7
0112830701	S005	S003	S004	2001-12-01	6	9	9
0122310101	-	-	S002	2000-03-27	-	-	10
0122310201	-	-	S002	2000-03-27	-	-	34
0122310401	-	S008	-	2000-03-28	-	6	-
0123720201	-	-	S004	2000-05-01	-	-	26
0123920101	-	-	S014	2000-05-18	-	-	16
0124300101	-	S001	-	2000-05-06	-	9	-
0125110101	-	S021	-	2000-05-24	-	14	-
0125320901	-	S015	S016	2002-12-17	-	10	10
0125910201	-	S007	S008	2002-06-17	-	13	13
0129321301	S002	-	-	2000-08-22	7	-	-
0134521601	S005	-	-	2002-06-18	21	-	-
0136540501	S008	S003	S006	2002-11-04	19	22	22
0136750301	U002	U002	U002	2001-05-22	25	30	30
0154150101	S003	U002	U003	2002-01-31	18	24	22
EF							
0134521701	S005	-	-	2002-11-15	15	-	-
0134720401	S005	-	-	2002-10-05	10	-	-
0160362601	S005	-	-	2003-08-02	18	-	-

NOTE. — Exp. time shows LIVETIME values for the central CCD and are shown only for the sets included in the sample. FF and EF show the Full frame and Extended full frame subsets

order to examine the variation of the spectral shape among the individual pointings, we renormalized the individual spectra so that their hard-band (10–14 keV for PN, 9.5–12 keV for MOS) count rates are the same as in the co-added spectrum. To avoid statistical scatter, we binned the spectra to better than 10% statistical accuracy in each bin. In the interesting 0.8–7.0 keV band (used below) the individual pointing spectra are consistent within 10% for each instrument (see Fig. 1 for PN). This stability is encouraging considering the background modeling. Furthermore, the co-added, renormalized spectra for the PN Full frame and Extended full frame modes are consistent with each other within a few % in the 0.8–7.0 keV band (Fig. 1). Thus, in the following we combine them in the single PN closed-cover spectrum.

The co-added PN (MOS) closed cover spectrum can be adequately fitted in the 0.5–14.0 (0.5–12.0) keV band with a model consisting of a broken power-law continuum and several Gaussians for the instrumental lines (see Fig. 2). For this fit, the model was not multiplied by the instrument effective area, only convolved with the energy redistribution matrix. At the low energies the photon indices and break energies of PN and MOS are similar ($\alpha_{soft} \sim 0.7-0.8$, $E_{break} \sim 1.3-1.5$ keV), while MOS spectra harden slightly more towards higher energies ($\alpha_{hard} = 0.4$ for PN and 0.1–0.2 for MOS).

4. FLARE FILTERING

The total EPIC background includes strong time-variable particle-induced component, i.e. flares. In the following we explore the flare filtering methods using the blank-sky data.

4.1. Blank sky data

TABLE 2
BLANK SKY SAMPLE

obs. ID	obs. start	t_{exp}	RA	DEC	filter			mode		NH	field
					PN	M1	M2	PN	MOS		
	year-mm-dd	ks	(J2000)	(J2000)						10^{20} cm^{-2}	
0098810101	2000-12-04	19	39.048	-52.321	T	T	T	FF	FF	3.0	WW Hor
0106660201	2000-11-18	45	333.882	-17.735	T	T	T	FF	FF	2.4	LBQS 2212-1759
0106660601	2001-11-17	96	333.882	-17.735	T	T	T	FF	FF	2.4	LBQS 2212-1759
0108060401	2001-07-27	32	53.117	-27.808	T	T	T	EF	FF	0.9	AXAF Ultra Deep F
0108060501	2001-07-27	43	53.117	-27.808	T	T	T	EF	FF	0.9	AXAF Ultra Deep F
0108060601	2002-01-13	53	53.117	-27.808	T	T	T	EF	FF	0.9	AXAF Ultra Deep F
0108060701	2002-01-14	78	53.117	-27.808	T	T	T	EF	FF	0.9	AXAF Ultra Deep F
0108061801	2002-01-16	51	53.117	-27.808	T	T	T	EF	FF	0.9	AXAF Ultra Deep F
0108061901	2002-01-17	41	53.117	-27.808	T	T	T	EF	FF	0.9	AXAF Ultra Deep F
0108062101	2002-01-20	50	53.122	-27.806	T	T	T	EF	FF	0.9	AXAF Ultra Deep F
0108062301	2002-01-23	75	53.117	-27.808	T	T	T	EF	FF	0.9	AXAF Ultra Deep F
0109660801	2001-06-12	57	203.654	37.912	T	T	M	FF	FF	0.8	Deep Field 1334+37
0111550101	2001-05-18	38	189.208	62.217	T	T	T	FF	FF	1.5	Hubble Deep Field N
0111550201	2001-05-18	37	189.208	62.220	T	T	T	FF	FF	1.5	Hubble Deep Field N
0111550401	2001-06-01	83	189.237	62.225	T	T	T	FF	FF	1.5	Hubble Deep Field N
0112370101	2000-07-31	48	34.500	-5.000	T	T	T	FF	FF	1.5	SDS-1
0112370301	2000-08-04	54	34.900	-5.000	T	T	T	FF	FF	1.5	SDS-2
0123700101	2000-04-27	40	163.179	57.480	T	T	TK	FF	FF	0.6	Lockman Hole

NOTE. — Exposure times are livetimes for the central PN CCD. “T”, “M” and “TK” denote the thin, medium, and thick optical filters. EF and FF denote the Extended full frame mode and the Full frame mode

Our blank sky data sample (Table 2) consists of 18 pointings with $N_H \leq 3 \times 10^{20} \text{ cm}^{-2}$ outside of the Galactic Spur with exposures longer than 20 ks, in which the resolved sources occupy an insignificant fraction ($< 1\%$) of the FOV.

Most of the blank sky observations in the sample are obtained with the “thin” optical filter (Ehle et al., 2004). We will restrict our analysis to the 0.8–7.0 keV band, in which the transparency of the thin filter differs from that of the “medium” filter by less than 2%. Thus, our results are applicable also to the medium filter data.

The PN sample consists of observations performed both in the Full frame and the Extended full frame readout modes. As mentioned above, the total internal background spectrum is consistent between the two modes. The total photon background is mainly affected by the telescope (effective area), filter (transmission) and CCD (quantum efficiency) which do not change between the PN modes. The slightly different uncorrected (see below) contribution of out-of-time events (Ehle et al., 2004) yields a negligible difference in the normalization of the total blank sky spectra between the Full frame and Extended full frame modes. Thus we do not separate the data in different PN modes in the analysis below, and our results are applicable to PN data obtained in both PN modes.

4.2. Hard band light curves

The standard method of selecting the quiescent periods for scientific analysis is to monitor the highest energies where the effective area for sky photons is very low (e.g., Arnaud et al. 2001; Lumb et al. 2002). In many XMM-Newton works, a fixed number (2–3) of standard deviations of the hard-band count rate distribution (e.g., Pratt & Arnaud (2002, 2003); Reiprich et al. 2003), or a fixed upper hard band count rate limit (e.g. Arnaud et al. 2001, 2002; Gastaldello et al. 2003) is used to accumulate the quiescent spectra. In order to obtain a large enough number of time bins for an adequate distribution, the time bin size in the above works is small, typically 100s. The resulting number of counts per bin is of the order of 10, and thus the statistical uncertainties of each bin are sev-

eral 10%. Thus, the 2–3 σ clipping corresponds to an upper filtering limit of 1.5–2.0 times the quiescent level, allowing possible low-flux flare contamination at this level.

It is entirely expected, and will be shown below, that such a background modeling uncertainty of up to a factor of 2 is too big for any accurate analysis of the low-brightness objects. Therefore, we instead use a fixed fraction of $\pm 20\%$ of the quiescent level for each pointing to define the hard band filtered quiescent periods GTI_q . The adopted limit of $\pm 20\%$ is a compromise between minimizing the allowed background variability and maximizing the final exposures. In order to minimize the loss of quiescent counts due to statistical uncertainties exceeding the 20% limit, we attempted to maximize the number of counts in each time bin. To this end, we used a time bin size of 1 ks. A possible drawback of using bigger time bin size is that very short flares will not be detected.

We also experimented with different choices for patterns and energy bins, and noted that a more strict set of choices (i.e. only single patterns and 10–12 keV band) only serves to reduce the number of counts with no improvement in the scatter of the renormalized blank sky spectra (see below). We thus chose to use the channels above 10 keV (PN) or 9.5 keV (MOS), up to the instrument’s internal upper limit, when extracting the hard band light curves (see Fig. 3 for PN). With these choices, the number of counts per bin is a few hundreds, and thus our adopted $\pm 20\%$ quiescence limits contain 2–3 σ of the rate distribution, so the statistical scatter above and below this threshold is negligible. In §7.3 we will examine the effect of using a higher limiting factor, similar to the commonly used filtering.

Our hard-band light curves show a wide variety of flaring activity, from none (ID 0098810101) to 60% of the total exposure time (ID 0112370301) affected by flares (see Fig. 3). The distribution of the count rates of the whole sample peaks at the low values, (see Fig. 4), implying a comparable quiescent level in all the pointings. The statistical errors of the rates in the 1ks time bins are 4–7%, while the centroids of the fitted Gaussians to the rate distributions of individual pointings

TABLE 3
QUIESCENT LEVELS

obs. ID	PN				MOS1				MOS2			
	hard		soft		hard		soft		hard		soft	
	cr cts s ⁻¹	t _{frac}										
0098810101	0.59	0.95	0.28	0.86	0.15	0.96	0.14	0.96	0.16	0.96	0.14	0.96
0106660201	0.63	0.57	0.28	0.50	0.18	0.66	0.14	0.49	0.18	0.74	0.14	0.53
0106660601	0.72	0.66	0.30	0.59	0.19	0.75	0.15	0.69	0.20	0.75	0.15	0.67
0108060401	0.62	0.35	0.28	0.31	0.18	0.38	0.14	0.35	0.19	0.35	0.14	0.32
0108060501	0.63	0.53	0.27	0.47	0.19	0.65	0.14	0.54	0.18	0.60	0.14	0.49
0108060601	0.72	0.70	0.29	0.62	0.21	0.74	0.15	0.74	0.21	0.71	0.15	0.69
0108060701	0.76	0.76	0.29	0.68	0.21	0.77	0.15	0.74	0.22	0.78	0.15	0.77
0108061801	0.70	0.58	0.28	0.51	0.20	0.71	0.14	0.60	0.20	0.72	0.14	0.62
0108061901	0.64	0.78	0.27	0.69	0.18	0.79	0.14	0.75	0.19	0.79	0.14	0.79
0108062101	0.62	0.66	0.27	0.58	0.17	0.82	0.14	0.78	0.19	0.84	0.14	0.82
0108062301	0.61	0.82	0.25	0.73	0.17	0.81	0.14	0.76	0.18	0.82	0.14	0.81
0109660801	0.66	0.50	0.28	0.44	0.18	0.58	0.14	0.52	0.19	0.61	0.14	0.54
0111550101	0.68	0.81	0.30	0.72	0.18	0.76	0.13	0.74	0.18	0.76	0.14	0.76
0111550201	0.68	0.64	0.28	0.57	0.18	0.67	0.13	0.67	0.18	0.72	0.13	0.70
0111550401	0.69	0.82	0.29	0.72	0.18	0.81	0.13	0.79	0.18	0.80	0.14	0.76
0112370101	0.62	0.54	0.26	0.47	0.16	0.66	0.13	0.53	0.17	0.69	0.13	0.50
0112370301	0.61	0.38	0.27	0.33	0.17	0.42	0.14	0.34	0.18	0.36	0.13	0.30
0123700101	0.67	0.45	0.29	0.40	0.20	0.67	0.16	0.63	0.20	0.53	-	-
mean	0.669	0.63	0.281	0.55	0.184	0.70	0.140	0.66	0.189	0.69	0.140	0.66

NOTE. — “cr” shows the mean count rates of the blank-sky sample in the full FOV in the hard band (“hard”) and in the 12–15 arcmin annulus in the soft band (“soft”), in the faint end (i.e., the individual quiescent levels). The count rate ranges used to determine the quiescent levels for the hard and soft bands are 0.54–0.80 cts s⁻¹ and 0.22–0.34 cts s⁻¹ for PN; 0.12–0.24 cts s⁻¹ and 0.10–0.18 cts s⁻¹ for MOS. Note that the count rate values don’t include the exposure correction. t_{frac} shows the fraction of useful exposure to total time after applying the hard-band ±20% filter, or with the double filter (“double”).

vary by 10–15%. This implies true variation of the quiescent flux with time at this level, presumably due to the variation of the cosmic ray intensity and/or the particle background (see De Luca and Molendi, 2004). Considering this variation, we chose to define the hard-band quiescent level as the mean (not exposure corrected, see §2) count rate in the faint end ranges of 0.540–0.800 cts s⁻¹ for PN and 0.120–0.240 cts s⁻¹ for MOS for each pointing. We used the ±20% limits around these levels to select the quiescent periods GTI_h (as explained above). Considering the full sample as a single long exposure, the average values in the above count rate ranges for PN, MOS1 and MOS2 are 0.669 cts s⁻¹, 0.184 cts s⁻¹ and 0.189 cts s⁻¹ in the hard band. These values are consistent with the non-simultaneous closed cover sample averages within the scatter (see §3).

The fraction of useful hard band filtered exposure time of the total sample is ~65% (~70%) for PN (MOS), and it varies between 40% – 100% in individual pointings. The co-added exposure times for the average blank sky spectrum (including exposure correction) are 630ks, 780ks and 750ks for PN, MOS1 and MOS2.

4.3. Mild flares

However, the exclusion of time intervals with elevated high-energy background rate turns out insufficient in many observations. During some quiescent periods, as determined by the hard band, the PN 1–5 keV count rate is high, reaching a factor of 3 times the quiescent level (see Fig. 5). To illustrate the spectra of the flares that may pass the high-energy filter, we selected the time periods GTI_{flare} with flares that are just above our factor of 1.2 cutoff but within a factor of 2 of the quiescent rate. The resulting co-added full FOV mild

flare spectra of the whole sample, following renormalization of the hard band count rate to unity, are substantially different from the quiescent spectra (Fig. 6). In particular, the mild-flare spectra are higher than the quiescent spectra by different factors at different energies, up to factors of 2.4 (PN) and 1.7 (MOS) at 2–3 keV.

To study the temporal stability of the above mild flare spectra, we split the individual pointings into ~10 periods containing ~5 ks of mild flare exposure. In order to ensure useful signal-to-noise ratio, we used large spectral bins of 0.8–2–4–7 keV. By subtracting the co-added blank sky spectra from the 5 ks mild flare spectra, we obtained the mild flare excess spectra, which we then renormalized to yield unity count rate in the hard band. Comparison of the renormalized mild flare excess spectra shows (Fig. 7) that the flares have highly variable spectral shape. The individual 5 ks spectra differ from each other more at lower energies, by a factor of 3–7 in maximum at 0.8–2.0 keV in different instruments.

Note that the full range of the flares shown in Fig. 7 would pass the hard-band filter if the upper limit is 2 times the quiescent level, which corresponds to that in many works that use the 2–3 σ clipping method. Thus, a more conservative filtering is necessary to select the quiescent data in order to minimize the time-variable flare component, which can give very different and unpredictable contribution in any given observation. The increasing temporal variability of the spectral shape of the mild flares towards the low energies indicates the need for better, soft-band based filtering (see also, e.g., Pointecouteau et al. 2004). We will do this in §4.4. If one wants to use the data obtained during mildly flaring periods, a more detailed method than simple rescaling of the quiescent background would be needed, which we will not attempt in

the current work.

4.4. Soft-band light curves

The obvious problem in using lower energies for flare filtering when analyzing a bright extended source, like a galaxy cluster, is the dominance of the source emission. However, the decline of the cluster brightness, as well as the decrease of the effective area with radius reduces the cluster contribution at the edge of the FOV. For example, for the bright nearby cluster A1795 in the 1–5 keV band, the cluster contribution in the $r = 12 - 15'$ detector region is less than 50% of the total emission (see §7.1). The absolute values of the $\pm 20\%$ variation of the blank sky quiescent level (see below) are thus 10–15% of the total quiescence level (A1795 plus the background) in the 1–5 keV band, or, greater than 2 times the statistical uncertainties. Thus, the soft-band filtering should be applicable to most clusters, except for the nearest ones like Coma.

Using our blank sky sample, we experimented with extracting light curves in different soft bands in the 12–15 arcmin annulus. We found that the 1–5 keV band is optimal for maximizing the number of counts in the 1 ks light curve bins while minimizing the scatter of the resulting filtered spectra. The 1–5 keV light curves are shown in Fig. 8. Similarly to the count rates in the hard band (§4.2), the resulting soft-band rate distribution of the whole sample has a well-defined peak at low values. We chose to define the soft-band quiescent level as the mean (not exposure corrected, see §2) count rate in the faint end ranges of 0.220–0.340 cts s^{-1} for PN and 0.100–0.180 cts s^{-1} for MOS1 and MOS2 for each pointing. The average count rate of all pointings in the above ranges are 0.281 cts s^{-1} (PN) and 0.140 cts s^{-1} (MOS1 and MOS2). Using the $\pm 20\%$ limits around the mean in the above count rate range for each pointing, we determined the soft band filtered quiescent periods GTI_s (see Table 3). Note that when applying the soft-band filtering to actual astronomical objects, the absolute value of the quiescent level in the soft band may of course include the source contribution. In order to achieve similar background accuracy as in this work, one should use the $\pm 20\%$ limits of the absolute values of our blank sky average, i.e. ± 0.056 cts s^{-1} (PN) and ± 0.028 (MOS1 and MOS2) cts s^{-1} around the (variable) quiescent level of a given object, when selecting quiescent periods (Appendix A).

Fig. 5 shows that the soft-band filtering is also very efficient in reducing the scatter in the hard band, which raises the possibility of using only on the soft-band light curve. However, there is residual hard-band variability due to non-simultaneous hard and soft flares. Thus, to remove all detectable flares, one has to apply both the $\pm 20\%$ hard-band filter and the $\pm 20\%$ soft-band filter (see Appendix A), which we define here as the “double-filtering” method. Note that the addition of the soft band filter results in only a 5–10% reduction of the clean exposure time, compared to that obtained with only the hard band filter (from 65% to 55% for PN and from 70% to 65% for MOS, see Table 3).

5. CONSTRUCTING THE TOTAL QUIESCENT BACKGROUND MODEL

We use here the double-filtered quiescent blank sky spectra, derived above, for a detailed investigation of the background modeling.

5.1. Count rate correlations

In order to construct a background model based on the blank sky data, we need to establish i) the stability of the

spectral shape of the total background and ii) a correlation between the count rates in the energy band used for the scientific analysis, and the background level indicator available in any extended source observation. The commonly used indicator is the count rate at the highest energies, where the source emission is eliminated due to negligible effective area. To achieve the above goals, we divided the double-filtered quiescent time periods for PN and MOS into 50–70 pieces each about 10 ks long, similar to the typical XMM-Newton observations. We extracted spectra obtained during the above periods, within the full FOV, and grouped the spectra into 0.3–0.8–1.0–2.0–4.0–7.0 keV energy bins (and the hard-band bins of 10–14 keV for PN and 9.5–12 keV for MOS), co-adding the MOS1 and MOS2 count rates to obtain spectra for MOS. These spectra have been compared to see if the background variations in different energy intervals are correlated.

5.1.1. 2–7 keV band

Figure 9 shows rates in our different 10 ks “observations” vs. the hard-band rate. Comparison of the data shows (see Fig. 9) that the count rates correlate better with the hard band rates at higher energies: the linear Pearson correlation coefficients (Neter et al. 1988) of the 2–4 and 4–7 keV rates with the hard band rates are 70% and 90% for PN, 85% and 95% for MOS, roughly consistent with Katayama et al. (2004). When the hard-band rate does not exceed the mean value by more than 10%, the 2–4 and 4–7 keV rates deviate from the hard-band based linear prediction (simple renormalization by the hard-band rate) with a standard deviation of $\sim 5\%$. This is similar to the scatter of the renormalized closed-cover spectra, implying that in this count rate range there is no significant excess background component in addition to the quiescent particle background. However, when the hard-band rate exceeds the average by more than 10%, the rates in the 2–7 keV band deviate downwards from the linear expectations (see Fig 9). This suggests a residual particle background with harder spectrum than that induced by the cosmic rays, perhaps due to the mild flares of the hard kind mentioned in §4.3, at a level below our filtering threshold.

5.1.2. 0.3–2.0 keV band

Below 2 keV, the count rates deviate more strongly from the linear expectation, reaching a maximum deviation of 50%, and a standard deviation of $> 20\%$, at 0.3–0.8 keV. The standard deviation of the rates around the linear expectation significantly exceeds that of the closed-cover sample at energies below 1.0 keV. Note that the variation of N_H in the sample ($0.6 - 3.0 \times 10^{20} \text{ cm}^{-2}$) yields only a 5% difference in the sky background (i.e. Galactic + extragalactic photon background) flux at 0.8–1.0 keV, and thus a negligible variation in the total background (see Fig. 2).

Based on the RASS count rates in the fields of the XMM-Newton pointings in our sample (see Appendix B), the spatially-variable Galactic background at these energies does not explain all of the above variation. This implies the existence of a time-variable background component below 1 keV, possibly due to another particle population and/or solar wind charge exchange background (indeed observed by *Chandra*, Wargelin et al. 2004). We did not find a practical way of incorporating the information on the spatio-temporal variability into the background modeling, and thus we will not go into more detail here.

5.2. Method

TABLE 4
BACKGROUND ACCURACY

R arcmin	hard band $\pm 50\%$ filter				hard band $\pm 20\%$ filter				double filter			
	band (keV)				band (keV)				band (keV)			
	0.8–1.0	1.0–2.0	2.0–4.0	4.0–7.0	0.8–1.0	1.0–2.0	2.0–4.0	4.0–7.0	0.8–1.0	1.0–2.0	2.0–4.0	4.0–7.0
PN												
0–10	46	32	28	16	31	18	17	12	24	12	10	7
10–15	39	28	23	16	29	19	17	13	20	11	8	5
0–15	42	30	26	16	30	18	16	12	22	12	8	6
MOS												
0–10	35	18	22	10	22	9	16	7	20	7	12	7
10–15	29	15	20	10	21	9	9	6	17	7	7	7
0–15	29	17	21	10	20	7	13	6	20	7	10	5

NOTE. — 90% confidence limits (%) for the relative background uncertainties, (prediction - data)/data, using the blank-sky sample. The columns “hard band $\pm 50\%$ filter” show values obtained using the $\pm 50\%$ limits in the hard band around the nominal level to filter the quiescent data, which approximates the method used in the literature. “hard band $\pm 20\%$ filter” refers to filtering the blank sky data with $\pm 20\%$ limits around the quiescent level in the hard band. “double filter” gives the values from our preferred method (see text). For the “hard band $\pm 50\%$ filter”, the simple scaling of the background model is used, while for the “hard band $\pm 20\%$ filter” and “double filter”, the 0.8–2.0 keV values are obtained without any renormalization and the 2.0–7.0 keV values are obtained with a maximum of 10% renormalization (see §5.2).

We use the hard band count rate to renormalize the blank sky spectrum to correspond to a given observation, unless the computed renormalization factor exceeds 1.1. In this case, we minimize the bias explained in §5.1.1 by using a maximum renormalization factor of 1.1.

Below 2 keV the count rates correlate very poorly with the hard band count rates, and thus a more detailed modeling would be favorable. However, since many of the deviations are below 10%, the spectrum of the excess on top of the blank sky based prediction is of too poor quality for proper spectral modeling, and we do not attempt it here. Rather, we exclude the energies below 0.8 keV from further analysis in order to minimize the complexity of the modeling, while maintaining enough counts for spatially resolved spectral analysis. We thus adopt the usage of the co-added blank sky spectrum for the 0.8–2.0 keV band as well, but without any renormalization. We will examine the effect of the above choices on the background prediction accuracy in §6.

In the actual extended source analysis we extract the blank sky spectra using the same detector region as used for extracting the source spectra (see Appendix A). The number of counts are often low in the hard band within a small region. Thus, to avoid statistical uncertainties, we further assume that the ratio of the observed hard band count rate to that of the blank sky spectrum is constant all across the detector, i.e. that the renormalization factor as derived from full FOV, i.e. of the pointing in question and the blank sky event file applies at all radii.

6. ACCURACY OF THE QUIESCENT BACKGROUND PREDICTION

For each blank sky observation, we form here a background model prediction in the 0.8–7.0 keV band following the recipe described in §5.2. By comparison of the background prediction with the observed blank sky spectrum, we evaluate the accuracy of the background modeling.

6.1. Individual pointings

We first extracted the full FOV spectra of the blank sky pointings (see Table 2) to maximize the signal-to-noise ratio in small spectral bins. For simplicity, we renormalized the full

band (0.8–7.0 keV) spectra using the hard band count rates (instead of using the maximum factor of 1.1 at 2–7 keV band, and no renormalization at 0.8–2.0 keV). The comparison of the PN and MOS background spectrum prediction of the individual pointings to the data reveals, that the background prediction of the hard-band-filtered spectra is consistent with the statistical uncertainties of 5% at 7.0 keV (see Fig. 10 for PN). The maximum inaccuracy increases towards lower energies, reaching 20% at 1.0 keV, and 40% at 0.8 keV, demonstrating the need for more complex modeling at lowest energies. The usage of the double filter (see §4.4) instead, improves the accuracy systematically (see Fig. 10). The accuracy of MOS1 and MOS2 is very similar, and thus in the following spectral analysis we use co-added MOS1 and MOS2 blank sky data to obtain results for MOS.

6.2. 10 ks spectra

In the following we examine the background accuracy with better temporal and radial resolution, in order to derive information more applicable to actual extended source analyzes. For the double-filtered data, we use the 10ks periods already introduced in §5.1, and we determine corresponding 10ks periods for the hard-band-filtered data. We extracted blank sky spectra in 0–10 and 10–15 arcmin annuli, around the center of FOV. We binned the spectra in the bins of 0.8–1.0–2.0–4.0–7.0 keV. We use the maximum renormalization factor of 1.1 in the 2–7 keV band, and no renormalization in the 0.8–2.0 keV band, as explained in §5.2.

6.3. Results

6.3.1. Hard band vs. double filtering

Comparison of the 10 ks PN spectra with the predictions using the hard band filter shows that the data deviate most from the prediction (by +60%) in the bin 1 of pointing 0106660201 and in the bin 3 of pointing 0112370101 (Fig. 3). In these periods there are some instants when the soft band count rate is elevated while the hard band appears consistent with the quiescent level. Thus the addition of the soft band filter cleans the data very efficiently resulting in 30% maximum relative uncertainties at 0.8–1.0 keV band. The hard-band-filtered MOS

data are overall in better agreement with the prediction and the addition of the soft band filter makes a smaller, but still systematic improvement (see Table 4).

We used the distribution of the data-to-model ratio for each energy to determine the 90% confidence limits for the background accuracy. We performed the calculation to both double-filtered, and hard-band-filtered data. Conservatively, we report the bigger of the positive and negative deviations. Considering the full FOV spectra, the addition of the soft band filtering improves the PN accuracy, compared to hard-band-only filtering, from 10–30% to 5–20% in the 0.8–7 keV band (see Table 4) at 90% CL, while MOS accuracy improves less significantly, staying at 5–20%. The accuracy of the double-filtered full FOV background of PN and MOS improves with increasing energy, from 20% at 0.8–1.0 keV to 5% at 4–7 keV. The accuracy improves systematically, but marginally, with increasing radius, suggesting that the residual flares are brighter in the middle of the FOV.

6.3.2. Uncertainty correlations

As shown above, the variable residual background components give different contribution in different bands, and thus the model uncertainties in the different bands are not strongly correlated (see Fig. 11). However, at the highest energies the correlations are stronger than at the lowest energies, implying an increasing complexity of the background modeling towards lower energies (as noted in §5.1.2, see also Appendix B).

To propagate accurately the model uncertainties to those of the final spectral fits (e.g., cluster temperatures), one needs to take into account these correlations. The most conservative approach would be to assume no correlation between the different wide bands and simply vary the normalizations of the background model in different bands by their 90% confidence level values (see Table 4), when evaluating the effect of the background uncertainties. This would result in extreme situations, e.g., with the $E < 2$ keV background at upper (lower) 90% CL limit, while the $E > 2$ keV background at lower (upper) 90% CL limit. Such situations would yield maximum variation in the temperature measurement, but fortunately the uncertainty correlations rule out such extremes (see Fig. 11). Thus, the inclusion of the uncertainty correlation information would result in smaller (and more correct) uncertainties in the resulting temperature measurements. Due to the large scatter and weak correlations, it is not practical to apply these results analytically to spatially resolved spectroscopy. Rather, in §7 we will describe a practical method to apply this information numerically.

6.3.3. Renormalization choices

We examine here the effect of our adopted choices of the maximum renormalization factor of 1.1 in the 2–7 keV band and no renormalization in the 0.8–2.0 keV band, on the accuracy of the prediction of the full FOV region background spectrum. For comparison of the resulting uncertainties with the above choices (derived above, see Table 4), we computed the uncertainties simply by renormalizing the co-added double-filtered blank sky spectrum in the full 0.8–7.0 keV band based on the hard band rate. The comparison shows (see Table 5) that our choice improves the modeling significantly, most importantly at energies below 2 keV.

6.3.4. Separating the particle background

TABLE 5
FULL FOV 90% CL ACCURACY

method	band (keV)			
	0.8–1.0	1.0–2.0	2.0–4.0	4.0–7.0
PN				
no separ., simple	29	18	11	6
no separ., impr	22	12	8	6
separ., impr	22	12	8	5
MOS				
no separ., simple	25	15	10	6
no separ., impr	20	7	10	5
separ., impr	20	7	7	5

NOTE. — 90% confidence limits (%) for the relative background uncertainties for full FOV region obtained with different renormalization methods and the double-filtered blank sky data. “separ” and “no separ” refer to separating or not the particle background before renormalization. “simple” refers to renormalizing the full band with the same factor, and “impr” refers to the method or using maximum factor of 1.1 in 2–7 keV band, and no renormalization in the 0.8–2 keV band.

When renormalizing the total co-added blank sky spectra with the hard band rate (consisting only of particle background), we effectively assume that the sky background spectrum of a given observation deviates from the sample average by the same factor as the particle background of a given observation deviates from the sample average. However, the sky background and the particle background are independent, and thus we would introduce a bias by the simple renormalization method. However, if we apply the renormalization only in the 2–7 keV band, where the sky background contributes only $\sim 20\%$, the effect of the bias should be negligible. To verify this, we computed the uncertainties of the soft-band-filtered background model, separating first the quiescent particle background (estimated from the closed-cover spectrum), renormalizing it by the hard-band count rate, and adding it back to the remaining sky background model. As expected, the resulting uncertainty values (see Table 5) for the full FOV are better than those for simple rescaling. However, they are not significantly different from those obtained with our adopted scaling method (see §5.2), which is much more practical.

7. APPLICATION TO A1795

To illustrate the application of the proposed background modeling procedure (See Appendix A), we analyzed the XMM-Newton observation 0097820101 of the bright nearby cluster of galaxies A1795, previously analyzed by Arnaud et al. (2001) and Nevalainen et al. (2002). The cluster was observed on 2000 June 26, with thin filters and in Full frame readout mode. We concentrate on regions outside the bright cool core ($r > 3$ arcmin) where the details of the background modeling are important. We processed the A1795 data using the same procedure as the blank sky data (§2). The LIVE-TIME values for different CCDs in a given instrument vary by less than 1%. At high energies, CCD 7 of MOS2 has a significantly higher count rate level, compared to other CCDs, so we excluded it. We further filtered the event files with expression “flag==0”, and including only patterns 0–4 (PN) and 0–12 (MOS). In 0.8–7 keV band, *epatplot* tool in SAS package shows that PN and MOS single and double pixel event distributions agree with the model used when generating the detector response matrices (Ehle et al., 2004).

TABLE 6
A1795 QUIESCENCE

Instr.	hard		soft		double
	cr	tfrac	cr	tfrac	exp
	[cts s ⁻¹]	[%]	[cts s ⁻¹]	[%]	[ks]
PN	0.697	28	0.560	23	10
MOS1	0.220	42	0.205	38	19
MOS2	0.190	38	0.166	34	17

NOTE. — “cr” shows the mean count rates of A1795 in the full FOV in the hard band (“hard”) and in the 12–15 arcmin annulus in the soft band (“soft”) in the faint end, i.e. the quiescent levels (see §4.2 and §4.4). MOS2 values are obtained excluding the spoiled CCD 7. The count rates are obtained using the light curves of 1 ks time bin, without applying exposure correction. “tfrac” shows the fraction of the selected good time intervals, compared to total, using the hard band light curves, and when applying the double filter (“double”). “exp” shows the resulting exposure time (including exposure correction) when applying the double filter

7.1. Light curves

Following the methods presented above, we extracted the PN and MOS light curves of A1795 in 1ks time bins in the hard band (> 10 keV for PN, > 9.5 keV for MOS) within the full FOV, and in the soft band (1–5 keV) within the 12–15 arcmin annuli, excising point sources (see Fig. 12). Consistently with the blank sky analysis, we do not apply the out-of-time correction at this stage to PN data (it will be applied later). Also, we report here the count rates as obtained from the light curves without applying an exposure correction (see Table 6), as in the case of the blank sky data (see §2).

In the hard band, using the same count rate range for averaging as for the blank sky (0.54–0.80 cts s⁻¹ for PN and 0.12–0.24 s⁻¹ for MOS1, see §4.2) we obtain quiescent levels of 0.697 s⁻¹ (PN) and 0.220 s⁻¹ (MOS1). Due to the exclusion of CCD 7 of MOS2, we lowered the nominal MOS2 limits by 15%, obtaining a quiescent rate of 0.190 cts s⁻¹. These are consistent with the largest deviation observed in the blank-sky sample. Using only periods when the count rate is within $\pm 20\%$ of the above levels, we determined the quiescent periods GTI_h. The hard band filter selects 30% (PN) and 40% (MOS) of the total exposure time.

In the 1–5 keV band in the 12–15 arcmin annulus of PN the cluster contribution is $\sim 50\%$ of the total A1795 count rate, while due to the smaller effective area the corresponding fraction is 30% in MOS1. Using the faint end count rate distributions (0.40–0.70 cts s⁻¹ (PN); 0.15–0.25 cts s⁻¹ (MOS1); 0.10–0.20 cts s⁻¹ (MOS2) we obtained the average quiescent (cluster + background) levels as 0.560 cts s⁻¹ (PN), 0.205 cts s⁻¹ (MOS1), 0.166 (MOS2). We used the absolute values of $\pm 20\%$ of the blank sky average (± 0.057 cts s⁻¹ for PN and ± 0.028 cts s⁻¹ for MOS1, see §4.4) around the above quiescent levels as the range to determine the quiescent periods GTI_s, except for MOS2, for which we used 15% smaller limits (± 0.023 cts s⁻¹) due to the exclusion of CDD 7. The useful exposure times using the double filter (i.e. using the common accepted times in GTI_h and GTI_s) reduce to 25%, 40% and 35% of the total for PN, MOS1, and MOS2.

Note that the application of only the soft band filter to PN data obtains 2 ks longer useful exposure than the application of only the hard band filter, i.e. in the case of A1795 the soft band filter is less effective than the hard band filter, in

TABLE 7
DOUBLE-FILTERED COUNT RATES IN THE HARD BAND

	A1795 cts s ⁻¹	<blank> cts s ⁻¹	renorm
PN	0.499±0.007	0.453±0.001	1.10±0.03
MOS	0.117±0.004	0.113±0.000	1.03±0.03

NOTE. — Count rates and 90% CL statistical uncertainties of A1795 and the blank sky (<blank>) in the 10–14 keV (PN) and 9.5–12 keV (MOS) bands for the double-filtered quiescent data in the full FOV, except that CCD 7 of MOS2 is excluded, and the renormalization factors (renorm). The values are obtained from the exposure-corrected spectra

cleaning the flares. This is due to the presence of flares with hard spectrum (see Fig. 12), which illustrates the need for double filtering.

7.2. Spectral analysis

We extracted the quiescent PN and MOS spectra in concentric annuli of radii 3–4–5–7–10–15 arcmin and in a full FOV circle, using the double filter (GTI_s and GTI_h, obtained in §4.4 and 4.2), excising point sources. We converted our background event files into sky coordinates of the A1795 observation and used the source region files in sky coordinates to extract the blank-sky spectra. The usage of the same region files minimized the differences in the size of the source and the background spectrum accumulation area below 1% level in our case. We co-added the MOS1 and MOS2 spectra (excluding MOS2 CCD 7), and averaged the responses. The exposure times are 10 ks and 36 ks for PN and the combined MOS spectra, respectively. Using the blank sky count rates of the double-filtered spectra of the full FOV in 10–14 keV (PN) and 9.5–12 keV (MOS) bands, we obtained the renormalization factors of 1.10±0.03 (PN) and 1.03±0.03 (MOS) at 90% CL (see Table 7). The uncertainties result from the statistical uncertainties of A1795 hard band counts rates of 2% (PN) and 3% (MOS). In the case of long A1795 observation these small uncertainties yield a negligible variation in the temperature measurements, compared to the other background modeling uncertainties (Table 8). In any given observation, this uncertainty should be evaluated and if significant, it should be propagated to the temperature measurements.

For PN, we generated the simulated out-of-time (OOT) event file as described in Ehle et al. (2004). We then subtracted the OOT spectra normalized by a factor of 6.3% (the ratio of CCD readout time to frame time in Full frame mode) from the cluster spectra. The subsequent subtraction of a not-OOT-corrected blank-sky spectrum normalized as described above would oversubtract the background, because the simulated OOT emission already includes 6.3% of it. Thus, before subtracting the blank-sky spectra, we have reduced their normalization calculated above, by 6.3%¹. This assumes that the background is spatially uniform so that randomization of one of the coordinates during the generation of the OOT event file does not change it. Given the small fraction of the OOT back-

¹ The background consists of observations performed in Full frame and Extended full frame readout modes and thus the exact reduction factor should be derived by averaging the corresponding readout time fractions (6.3% and 2.3%) using exposure times as weights. However, we show in Appendix C that approximating the exact factor by 6.3% results in negligible effect on A1795 temperature measurements

TABLE 8
TEMPERATURES

R arcmin	double filtered			hard band $\pm 50\%$	
	T [keV]			T [keV]	
	stat	exact	appr	stat	exact
PN					
3–4	5.4[5.1–5.8]	5.4–5.5	5.4–5.5	5.3[5.1–5.5]	5.2–5.4
4–5	5.0[4.7–5.5]	5.0–5.1	5.0–5.1	5.2[4.9–5.5]	5.0–5.3
5–7	5.2[4.8–5.6]	5.1–5.4	5.1–5.4	5.1[4.9–5.4]	4.7–5.4
7–10	4.7[4.3–5.3]	4.4–5.1	4.4–5.1	5.2[4.8–5.6]	4.0–6.1
10–15	4.3[3.5–5.4]	3.5–5.5	3.3–5.6	4.2[3.6–5.1]	2.0–8.2
MOS					
3–4	6.0[5.7–6.3]	5.9–6.0	5.9–6.0	6.0[5.7–6.2]	5.8–6.0
4–5	6.0[5.6–6.4]	5.9–6.1	5.9–6.1	5.9[5.7–6.2]	5.7–6.0
5–7	5.8[5.5–6.2]	5.6–6.0	5.7–6.0	5.8[5.6–6.1]	5.3–6.1
7–10	5.6[5.1–6.2]	5.0–6.0	5.1–6.2	5.8[5.4–6.3]	4.4–6.8
10–15	4.9[4.2–5.8]	3.6–6.0	3.5–6.8	5.3[4.6–6.2]	2.2–9.3

NOTE. — The PN and MOS temperature profile values of A1795 obtained using the double filtering method (“double filtered”) or using the approximated fixed σ clipping method (“hard band $\pm 50\%$ ”). “stat” shows the best fit temperatures in the 0.8–7 keV band with statistical uncertainties. The variation of the best-fit temperature when including the background uncertainty correlation information using the exact method (§7.2.1) is denoted as “exact”, and the variation resulting from the approximate background uncertainty propagation method is denoted as “appr” (§7.2.2). Note that the systematic uncertainties “exact” and “appr” are independent of the statistical uncertainties in the column “stat”. The uncertainties are reported at 90% confidence level

ground, this is a reasonable approximation (see Appendix C).

For spectral fits, we excluded the energy interval 1.45–1.55 keV which contains time-variable Al K instrumental lines. Exclusion of this band is also necessary in order to avoid incorrect spatial localization of instrumental Al lines due to the not corrected OOT effect on the background data. To propagate the different background uncertainties at different energies, and to perform the background model renormalization in an energy-dependent manner (specifically, only in the 2–7 keV band), we divided each spectrum into 4 bands, 0.8–1–2–4–7 keV, and treated them as separate spectra with tied model parameters (see Appendix A). We calculated the background normalization taking into account the above renormalization factors and the OOT correction (see Appendix A). The PN and combined MOS spectra of the cluster were fit with a MEKAL model and Galactic absorption with $N_H = 1.0 \times 10^{20} \text{ cm}^{-2}$. The resulting best-fit temperatures in different radial bins are given in Table 8 and in Fig. 13. There is some evidence of multiple thermal components at the same radii (as noted, e.g., by Nevalainen et al. 2003, when including the lowest energies 0.3–0.8 keV in the fit). This may be part of the reason why the PN best fit values are systematically lower than those of MOS (see Table 8). However, the single temperature model is adequate for our present purpose of studying the background systematics.

7.2.1. Exact propagation of the background uncertainties

We will first try to include the background uncertainties into the temperature fits using the full information on uncertainty correlations obtained from our sample of blank-sky spectra (see §6.3.2). Each 10 ks blank-sky spectrum corresponds to a different realization of the background scatter in different

bands, which we use to modify the normalization of the background model in each band. We fitted the A1795 spectra using the background normalizations calculated from each of the 10 ks blank-sky piece, and used the resulting distribution of the best-fit temperatures to derive the systematic effect of the background uncertainty for each radial bin.

Due to its larger effective area, the cluster signal in PN is relatively stronger, compared to the background, than in MOS. Therefore the background uncertainties have a bigger effect on MOS than on PN (see Table 8). The increasing fraction of the background with the larger radius increases the background-induced uncertainty in the best-fit T from a few % (90% CL) at $r = 3–4'$ to $\sim 20–25\%$ (i.e., $\sim \pm 1$ keV for A1795) at $r = 10–15'$ (Fig. 13). Thus, even though the systematic uncertainties exceed the statistical ones ($\sim 20\%$) at 10–15 arcmin, they do not prohibit the derivation of cluster temperature profiles at $r > 10'$ — provided the flares are cleaned conservatively as we do in this work.

7.2.2. Approximate propagation of the uncertainties

To reduce the complexity of the fitting procedure, we sought a simpler error propagation method approximating the above effect on the temperatures. We found that if we vary the background model simultaneously in the full 0.8–7.0 keV band by $\pm 10\%$, the scatter of the best-fit temperatures is quite close to that obtained using the full uncertainty correlation information (see Table 8). The only significant difference is the MOS temperature at 10–15 arcmin, whose 20% uncertainty is overestimated as 40%. This may be due to the larger background-to-source flux ratio in MOS than in PN (see Section §7.2.1). Basing only on one cluster we cannot estimate how well the approximation works in different clusters. However, it is reasonable to assume that the approximate method yields conservative estimates on the uncertainties. Thus, if the approximate method yields uncertainties that are too large for the scientific goals when analyzing a given object, one could perform the more complicated exact error propagation method, to decide whether meaningful results can be derived for the object in question.

7.3. Comparison with flare cleaning from the literature

It is useful to compare the temperature uncertainties obtained with our method of flare filtering (double filter using the $\pm 20\%$ limits), with those obtained with the less restrictive flare filtering method commonly used in XMM-Newton cluster work (e.g., Pratt & Arnaud 2002, 2003; Reiprich et al. 2003). To do this, we repeated our A1795 analysis using only the hard band for flare filtering and increasing the light curve clipping limits to $\pm 50\%$ around the quiescent level (the actual clipping limits used in those works are 50–100%, see §4.2, so our derived uncertainties will in fact be lower limits). We also have re-created the blank-sky datasets, a combined one and one divided into 10 ks pieces, using a similar, less restrictive flare cleaning. We then used the hard-band rate to renormalize the background model in the whole energy band and compared it with the 10 ks background pieces to obtain the uncertainty distributions. As expected, the background scatter is significantly greater than in our method, because of the inclusion of higher levels of the the spectrally variable flare emission (see §4.3). The scatter reaches $\pm 45\%$ in the lowest energy bands (see Table 4).

We then included the resulting background uncertainty correlations into the A1795 spectral fits (§7.2.1). The results are

shown in Fig. 14. At $r > 5'$, the systematic temperature uncertainties in the common method are 2–4 times as large as those in our method. At $r > 10'$, these uncertainties become so large (50–100% for PN, 60–80% for MOS) that they render the temperatures essentially unconstrained. This is despite the shorter clean cluster exposures that we used. This comparison emphasizes the importance of the conservative flare filtering when fitting spectra of low-brightness cluster regions.

8. CONCLUSIONS

We analyzed samples of XMM-Newton EPIC blank-sky and closed-cover data in order to explore the background subtraction methods for such extended sources which fill the whole EPIC FOV and thus render the local background estimation difficult. We found that during some quiescent periods, as determined by the hard band, the 1–5 keV band count rate reaches a factor of 3 times the quiescent level. Similarly, during some quiescent soft band periods, there are hard flares. Due to these non-simultaneous hard and soft flares, we adopt the use of double filtering, i.e. discarding the time periods when either the hard-band or the soft-band light curves show excess by more than 20% over the nominal rate. If using only the outer part of the FOV (12–15 arcmin) the cluster contribution is small enough for the soft band filtering to be feasible.

The method for quiescent background estimation in our work is to use the filtered average blank sky spectrum in a given region, and to renormalize it to match the hard band count rate of a given observation. The blank sky data show that there is a poor correlation between the hard band (above 10 keV) and the useful 0.8–2.0 keV band, indicative of a remaining soft background component. Further, we found that when the hard band rate exceeds the average by more than 10%, the 2.0–7.0 keV band excess remains at 10%, indicative of an additional background component with harder spectrum than that of the quiescent particle background. Thus, in order to minimize the uncertainties of our modeling, we adopt a method of not renormalizing the background below 2 keV,

and for the higher energies, using a maximum of 1.1 for the renormalization factor.

Comparing the above models with the blank sky data, we determined the accuracy of the background modeling. Using the double-filtering method, we obtain a 90% CL uncertainty for the model background rate of ± 5 –20%, for both MOS and PN. Indicative of the higher variability of the particle-induced background at lower energies, the accuracy decreases from $\pm 5\%$ at $E = 4$ –7 keV to $\pm 20\%$ at $E = 0.8$ –1 keV. This compares to a 10–30% respective PN uncertainty when only the hard-band light curve is used for filtering, and to a 15–45% PN uncertainty when applying the commonly used 2–3 σ filtering method. The improvement in the background modeling accuracy, when adding the soft-band filter, results in only a 5–10% reduction of the useful exposure time.

Based on our analysis of a nearby bright cluster of galaxies A1795, the effect of the background uncertainties on the temperature measurement, increase from a few % at 3–4 arcmin to 20–25% (i.e. ~ 1 keV for A1795) at 10–15 arcmin. A conservative approximation of the commonly used 2–3 σ clipping method using the hard band light curve in XMM-Newton works, yields that the resulting increased background uncertainties due to the allowed spectrally variable flare emission, render the temperatures essentially unconstrained at radii above 10 arcmin in A1795. Thus, the background uncertainties do not prohibit the EPIC temperature profile analysis of low-brightness regions, like outer regions of galaxy clusters, provided a conservative flare filtering such as the double filtering method with $\pm 20\%$ limits is used.

We thank Drs. J. Huovelin and H. Katayama and the referee, Dr. S. Molendi for useful comments. JN acknowledges support by NASA grants NAG5-9945 and NAG5-13250; MM was supported by NASA contract NAS8-39073. Thanks to Dr O. Vilhu for his support. Thanks to Merilä family for hospitality.

REFERENCES

- Arnaud, M., Neumann, D., Aghanim, N., et al., 2001, *A&A*, 365L, 80
 Arnaud, M., Majerowicz, S., Lumb, D., et al., 2002, *A&A*, 390, 27
 De Luca & Molendi, 2002, in “New Visions of the X-ray Universe in the XMM-Newton and Chandra era”, astro-ph/0202480
 De Luca & Molendi, 2004, *A&A*, 419, 837
 Ehle, M., Breittfellner, R., González Riestra, R., et al., 2004, “XMM-Newton Users’ Handbook”
 Gastaldello, F., Ettori, S., Molendi, S., et al., 2003, *A&A*, 411, 21
 Katayama, H., Takahashi, I., Ikebe, Y. et al., 2004, *A&A*, 414, 767
 Lumb, D., Warwick, R., Page, M., et al., 2002, *A&A*, 389, 93
 Marty, P., Kneib, J-P., Sadat, R., et al., 2003, *SPIE*, 4851, 208
 Neter, J., Wasserman, W. & Whitmore, G.A., 1988, *Applied Statistics* (third edition), Newton, Massachusetts: Allyn and Bacon, 1988. ISBN 0-205-10328-6
 Nevalainen, J., Lieu, R., Bonamente, M., & Lumb, D., 2003, *ApJ*, 584, 716
 Pointecouteau, E., Arnaud, M., Kaastra, J. & de Plaa, J., 2004, *A&A*, 423, 33
 Pratt, G. & Arnaud, M., 2002, *A&A*, 394, 375
 Pratt, G. & Arnaud, M., 2003, *A&A*, 408, 1
 Read, A. & Ponman, T., 2003, *A&A*, 409, 395
 Reiprich, T., Sarazin, C. & Kempner, J., 2003, *ApJ*, 608, 179
 Snowden, S., Egger, R., Freyberg, M. et al., 1997, *ApJ*, 485, 125
 Snowden, S., Egger, R., Finkbeiner, D. et al., 1998, *ApJ*, 493, 715
 Wargelin, B., Markevitch, M., Juda, M., et al., 2004, *ApJ*, 607, 596
 Zhang, Y.-Y., Finoguenov, A., BÄuhringer, H., et al., 2004, *A&A*, 413, 49

APPENDIX

A. BACKGROUND SUBTRACTION METHODS

Here we summarize our method for spatially resolved spectroscopy of extended sources in the 0.8–7 keV band. It can be used for observations with Thin and Medium optical filters in Full frame and Extended full frame readout modes.

1) *Flare filtering.* We use the full FOV, hard-band ($E > 10$ keV for PN, $E > 9.5$ keV for MOS) cluster light curve (patterns 0–4 for PN, 0–12 for MOS) to determine a first-approximation quiescent level as a count rate averaged in the range 0.54–0.80 cts s⁻¹ (PN) and 0.12–0.24 cts s⁻¹ (MOS1 and MOS2). All light curves should be binned into 1 ks bins to ensure sufficient statistics. If there are no time bins where the count rate is within the above ranges, the background differs significantly from that in our sample, and thus our results cannot be applied. If any inactive detector regions or the peculiar CCDs significantly reduce the size of the useful detector area (from 615 arcmin⁻² for PN and 656 arcmin⁻² for MOS1 and MOS2 that we used in the blank sky sample), one needs to reduce the above count rate limits accordingly. We then determine the hard-band quiescent periods GTI_h allowing the light curve to vary within $\pm 20\%$ of the quiescent level.

Then we use the $r = 12 - 15'$ (from the center of the FOV), $E = 1 - 5$ keV light curve to determine the soft-band quiescent level. This value contains source emission, and therefore varies depending on the source. We use the Gaussian peak in the faint end of the count rate distribution to determine the quiescent level. If there are not enough time bins for a proper distribution, we define the quiescent level so that the lower 20% limit matches the minimum count rate. The soft-band quiescent periods GTI_s are determined by allowing the count rate to vary around the above-determined value (that may include source emission) within $\pm 20\%$ of the absolute values of the average blank-sky soft-band count rates of ± 0.056 cts s⁻¹ (PN), or ± 0.028 cts s⁻¹ (MOS1 and MOS2). If these limits are smaller than the 2σ statistical uncertainties of the quiescent level (in the case of a very bright source), one has to use only the hard band filter. We then apply both GTI filters simultaneously, e.g., using the following option in `evselect`: `expression='GTI(GTIh,TIME)&>I(GTIs,TIME)'`.

A blank-sky dataset cleaned of flares in exactly such a manner is available at <http://www.astro.helsinki.fi/~jnevalai/XMMbkg/>.

2) *Background.* We calculate the sky coordinates of the combined blank-sky event file to match those of the cluster pointing, and extract the blank-sky spectra in the same sky regions as used for the data. The MOS1 and MOS2 spectra are co-added for the source as well as the background.

3) *Background normalization.* We compute a background renormalization factor by obtaining the count rate in the hard band (10–14 keV for PN, 9.5–12 keV for MOS), full FOV, flare-filtered spectrum of the source in question, and dividing it by the corresponding value in the co-added blank-sky spectrum. This factor is applied to the background model at $E > 2$ keV. If it exceeds a factor of 1.1, we use 1.1 in this band. For $E < 2$ keV, we always use 1.0 (see §5.2). For PN Full frame data, we reduce the obtained renormalization factor by 6.3% to account for the background fraction subtracted as part of the OOT correction. If the size of the accumulation region of the source and the background region differs significantly, we adjust the renormalization factor further.²

4) *OOT correction.* For PN Full-frame data, we generate a simulated OOT event file and extract the spectra with the same GTI and region choices as for the source, and subtract the properly normalized OOT spectra from the source spectra.

5) *Spectral fitting.* In XSPEC, we input the source spectrum as four separate datasets, and in each one, use only photons in one of the four bands 0.8–1–2–4–7 keV (excluding the 1.45–1.55 keV band due to variable Al K lines). We set the BACKSCAL keyword in the background spectrum files to the inverse of the renormalization factors calculated at step 3 (note that they are different for $E < 2$ keV and $E > 2$ keV). Model parameters should then be tied equal in all four sets to obtain a best-fit temperature and its statistical uncertainty.

6a) *Systematic uncertainty, approximate estimate.* Keeping the set-up from 5), we input the original blank-sky spectrum in XSPEC as “corfile” for each of the four datasets, and fit the data with all “cornorm” values set to 0.1 and then to -0.1. The resulting difference in the best-fit temperature can be taken as a 90% CL estimate of the systematic uncertainty. This method may overestimate the background uncertainties, especially for MOS data at large radii. Thus, if smaller uncertainties are desired, one may use step 6b instead. If this accuracy is sufficient, instead of 4 energy bands at step 5, one can use just two bands, 0.8–2–7 keV.

6b) *Systematic uncertainty, exact estimate.* Instead of using the same “cornorm” of ± 0.1 in all bands, we can use the uncertainty correlation information to change the “cornorm” values in each of the four bands individually, calculated from our 10 ks blank-sky pieces (see the above website for this dataset). A distribution of the best-fit temperatures obtained using each set of “cornorms” can then be used to derive the 90% CL interval for the systematic uncertainty.

² Note that the `backscale` tool in SAS distribution `xmmsas_20030110_1802-5.4.1` yields correct values for the provided co-added blank sky event file only when using the region expressions in detector coordinates (DET_X,DET_Y).

B. BACKGROUND COMPONENTS AT $E < 2$ KEV

Here we examine the EPIC background components at the lowest energies. Below 2 keV, the sky background becomes important, compared to the particle induced background. The sky background consists mainly of Galactic background and the extragalactic emission due to unresolved point sources. The extragalactic component above $E=0.8$ keV is spatially uniform and has a spectral shape of $\alpha_{ph} = 1.4$. However, the Galactic emission and absorption vary between the different pointings.

To estimate the contribution of different background components at $E < 2$ keV in our sample, we analyzed the co-added full FOV PN and MOS double filtered quiescent spectra (from §4.4). After subtracting the co-added closed-cover spectrum (§3), we modeled the sky background spectrum, following Snowden et al. (1998), as a power-law with the photon index of 1.4 (extragalactic background) and two thermal components. The best fit (Fig. 2) shows that at 1.0 keV the extragalactic emission is comparable to that induced by the cosmic rays, while the Galactic emission is negligible (note that all our blank-sky fields are outside the bright Galactic features). Towards lower energies the Galactic emission becomes significant: at 0.8–1.0 keV, it comprises 15% of the total background emission.

We used the ROSAT All Sky Survey data (Snowden et al. 1997) to obtain the 0.6–1.2 keV surface brightness for the different pointing directions in our sample, obtaining a standard deviation and maximum deviation from the mean of 10% and $\pm 20\%$, respectively. This level of variation in the total sky background is substantial, but does not account fully for the variation at these low energies that we observe. Thus, in addition to the variation in the Galactic emission, there should be another variable emission component contributing significantly at energies below 1 keV in our sample, probably residual background flares with a soft spectrum.

C. OUT-OF-TIME CORRECTION TO THE BLANK SKY DATA

Since the PN Full frame source spectra must be corrected for the out-of-time (OOT) effect, for consistence this correction should also be applied to the blank sky data (the exact method). However, we assumed in this work that the net OOT effect on the background emission in a given region can be approximated by the increase of the normalization by 6.3% in the Full frame mode. This approximation was motivated by the small fraction of the OOT events, and by the spatial and spectral uniformity of the background emission. Here we examine in detail the accuracy of this approximation.

First, to obtain results using the exact method, we separated a Full frame mode subset from our blank sky sample before co-adding the individual blank sky spectra. We produced the OOT event files corresponding to these Full frame mode blank sky pointings, and co-added them into a single OOT event file. Using the same selection criteria as for the observed background spectra, and the co-added Full frame OOT event file, we extracted the OOT blank sky spectra. After scaling them by 0.063, we subtracted them from the observed background spectra, producing thus OOT corrected background spectra for the Full frame mode. We used the hard band of the full FOV spectrum of the OOT corrected background and A1795 to obtain the renormalization factor. After adjusting the background spectra with this factor, we subtracted them from the OOT corrected A1795 data and fitted the resulting spectra.

Then, we approximated the above exact procedure by following the method used in this paper, i.e using the total co-added blank sky sample (including data obtained in both Full frame and Extended full frame modes) without performing any OOT correction. The subtraction of the hard-band-renormalized (see above), not-OOT-corrected blank sky spectrum oversubtracts the background, because both the simulated out-of-time emission of A1795 and of the co-added blank sky spectra contain a out-of-time contribution due to the background. Thus, before subtracting the not-OOT-corrected blank sky spectra from OOT-corrected A1795 spectra, we reduced the background normalization by 6.3%. Fitting the data shows that the obtained temperatures agree with those derived using the above exact method within 0.1 keV at all radii. Thus, it is justified to reduce the complexity of the analysis with the approximation discussed here, i.e. approximating the OOT effect on the background by reduction of the normalization of the not-OOT-corrected background by 6.3% for any Full frame mode observation.

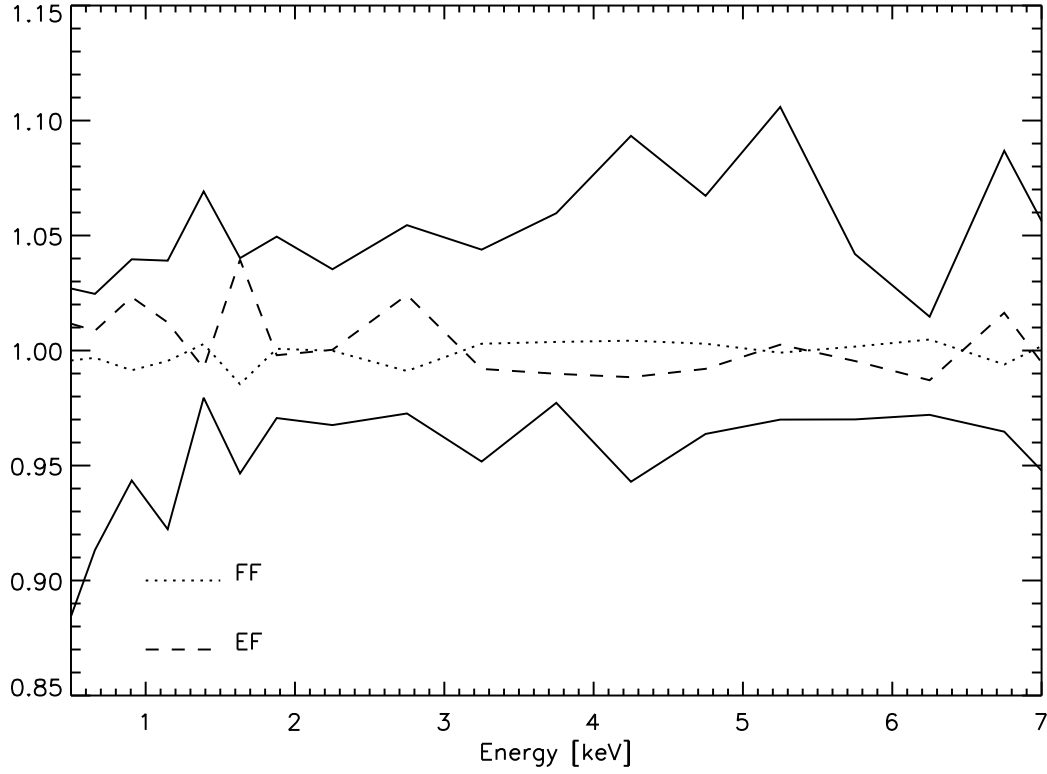


FIG. 1.— Solid lines show the relative deviation of the individual renormalized closed-cover PN spectra from the average at 90% CL. The ratio of the renormalized average Full frame (FF) and Extended full frame (EF) spectra to the sample average are shown as dotted and dashed lines, respectively

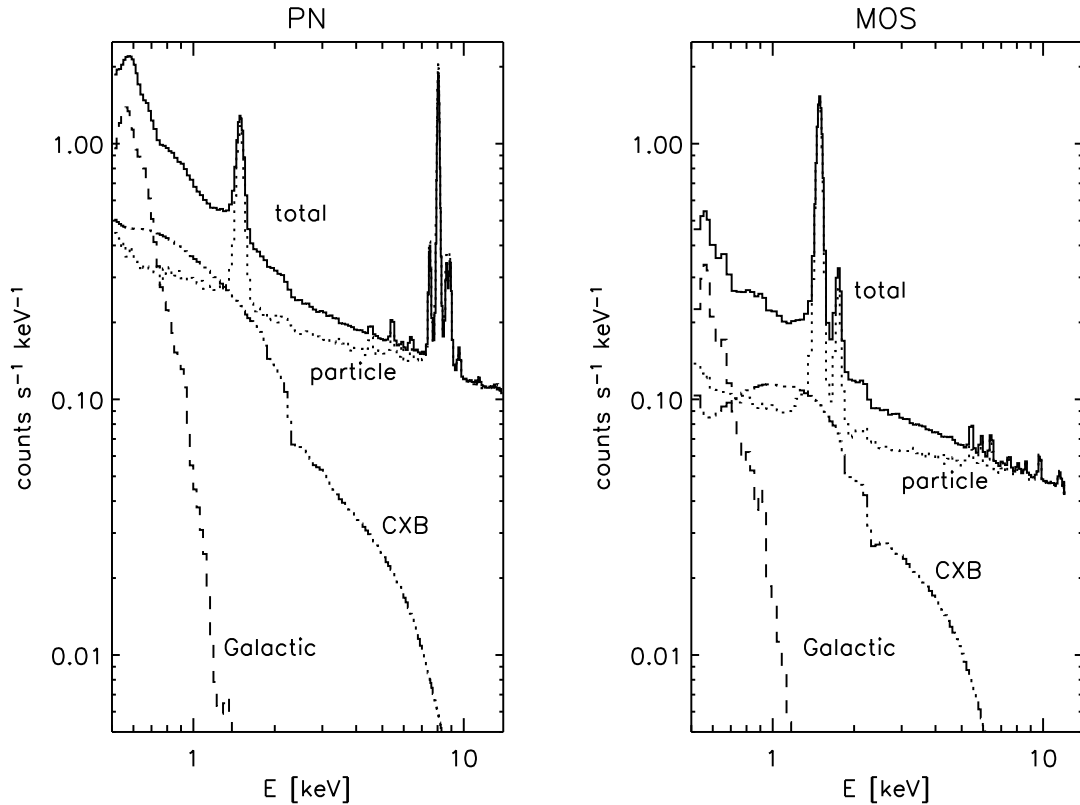


FIG. 2.— The total quiescent PN and MOS background and convolved components as obtained from the full FOV spectra of the co-added closed-cover data sets (“particle”) and from the double-filtered (see §4.4) blank sky data sets (“CXB” and “Galactic”)

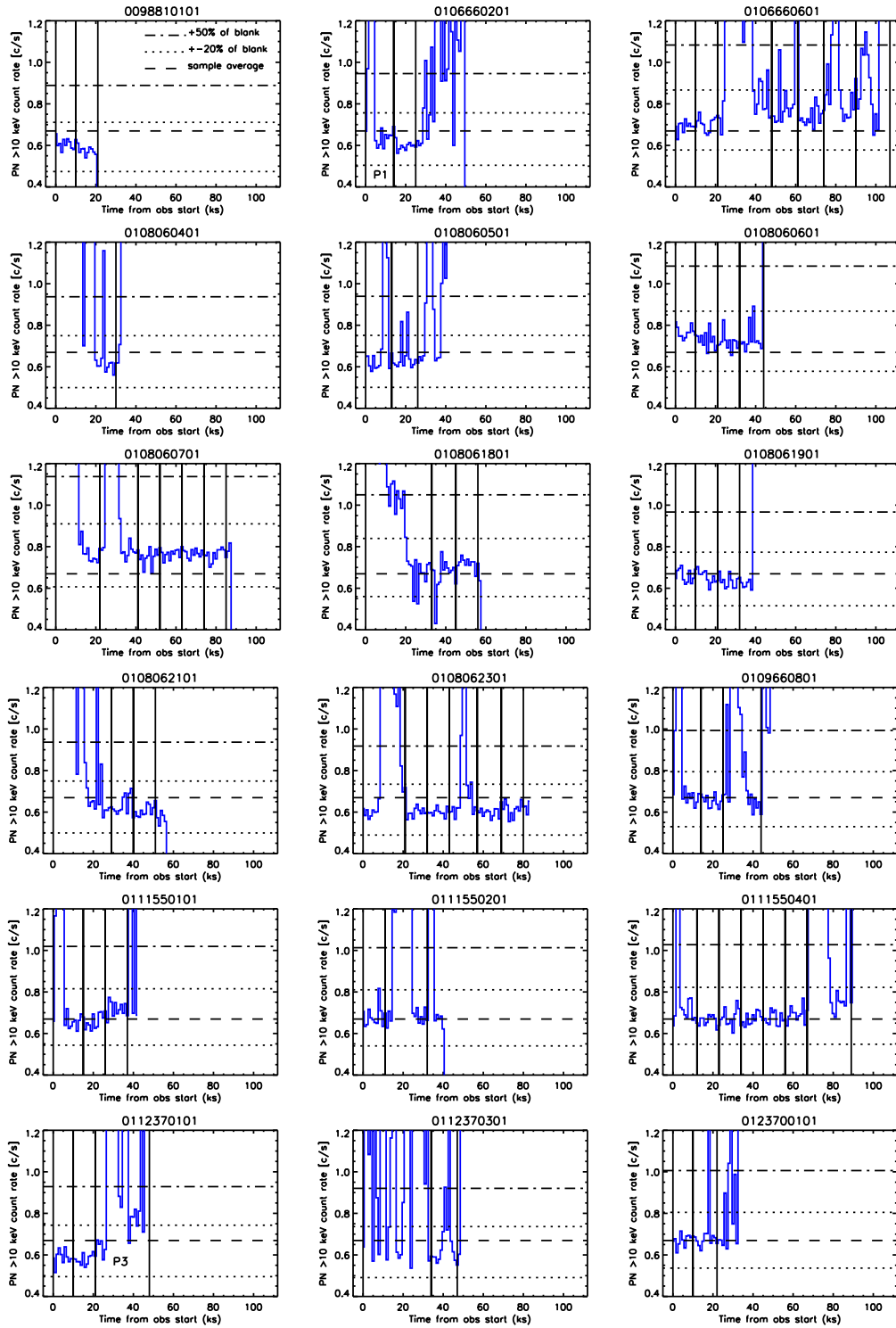


FIG. 3.— EPIC PN $E > 10$ keV, full-FOV light curves in 1 ks bins for the observations listed in Table 2, together with the sample-average quiescent rate (dashed line), the $\pm 20\%$ limits around the individual mean (dotted line), and a level exceeding the quiescent by 50% (dash-dot line). The vertical lines show the start and stop times of the 10 ks periods used in the analysis. P1 (in 0106660201) and P3 (in 0112370101) mark the specific periods discussed in the text.

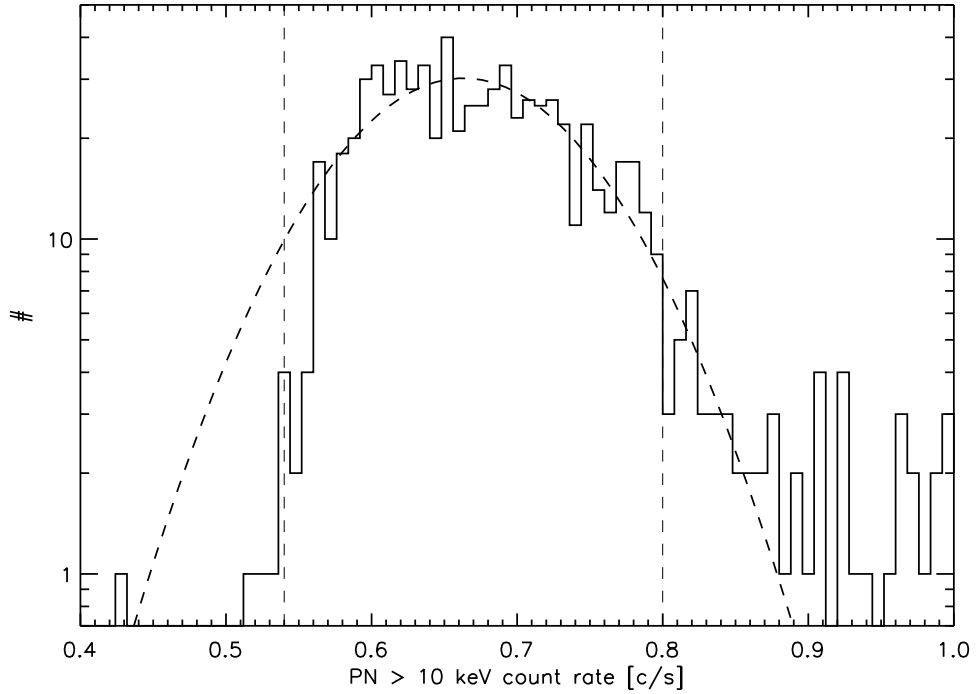


FIG. 4.— The distribution of PN $E > 10$ keV counts of the blank-sky sample in 1 ks time bins, with a best-fit Gaussian (dashed curve). The range chosen to determine the quiescent levels in the blank sky pointings ($0.54\text{--}0.80$ cts s^{-1}) is shown by vertical dashed lines.

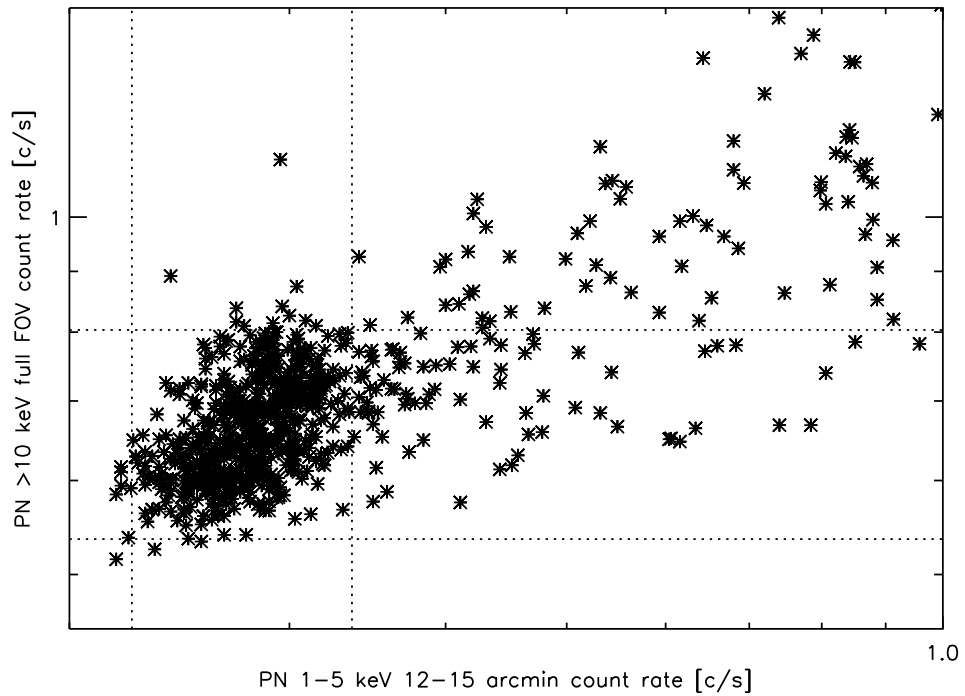


FIG. 5.— The faint end of the not flare-filtered PN count rates of the blank-sky sample in 1 ks time bins, in the 1–5 keV band for the 12–15 arcmin annuli and in the $E > 10$ keV band for the full FOV. Our adopted ranges for determining the quiescent levels in the blank sky pointings ($0.22\text{--}0.34$ cts s^{-1} in the soft band; $0.54\text{--}0.80$ cts s^{-1} in the hard band) are shown by dotted lines.

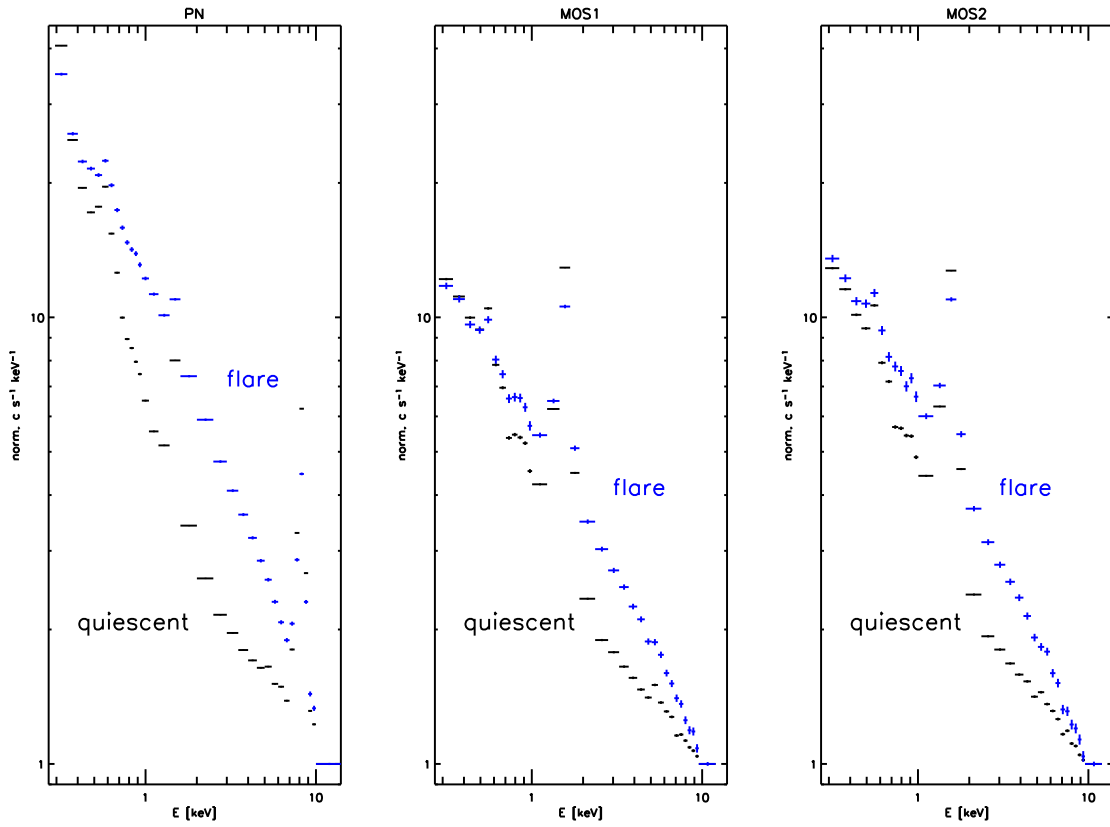


FIG. 6.— The co-added, hard-band-filtered quiescent full FOV spectra (black) and the “mild flare” spectra (blue), renormalized to 1 in the hard band. The mild flare spectra are selected using periods when the hard-band count rate exceeded the quiescent level by a factor between 1.2 and 2.

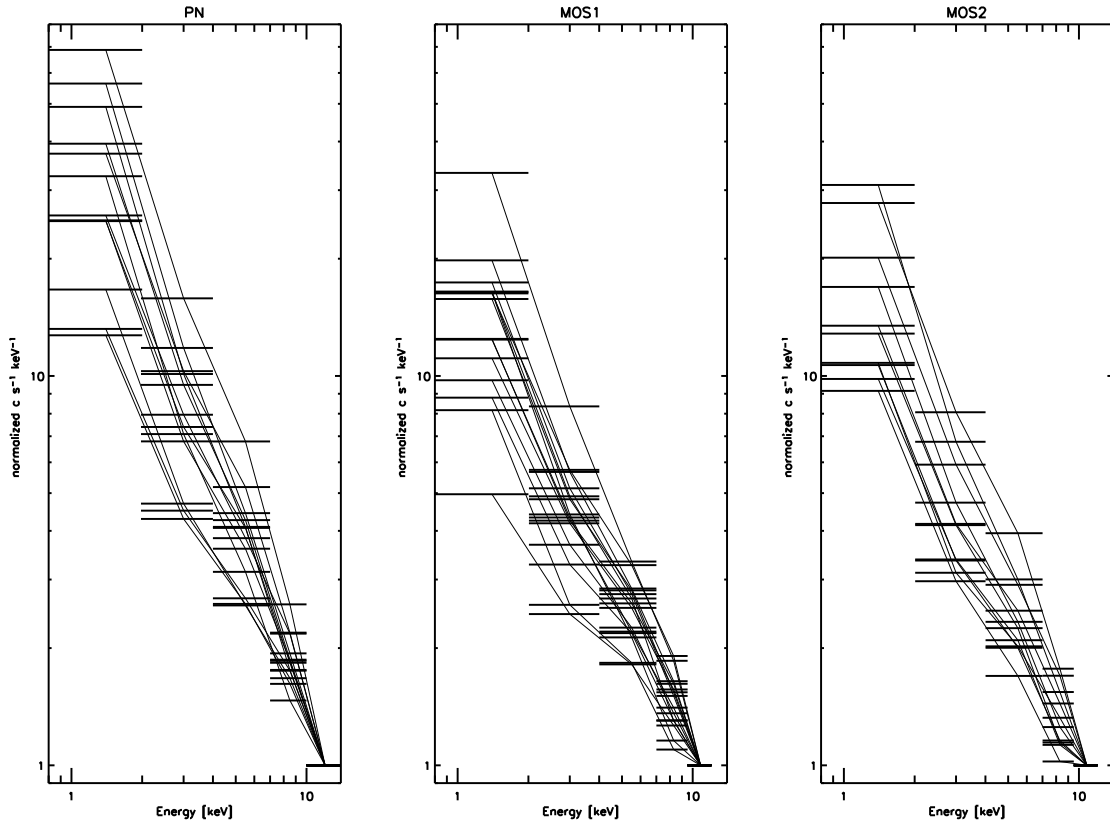


FIG. 7.— The mild-flare excess spectra (i.e., the mild flare spectra minus the quiescent spectra, see §4.3) normalized to unity at 10–14 keV (PN, left panel) or at 9.5–12 keV (MOS1 and MOS2, middle and right panels). The quiescent spectra are obtained by the $\pm 20\%$ filter while the mild-flare periods are selected by applying the factor 1.2-2 filter in the hard band (as in Fig. 6). The time intervals are selected in such a way that each spectrum has about 5 ks exposure.

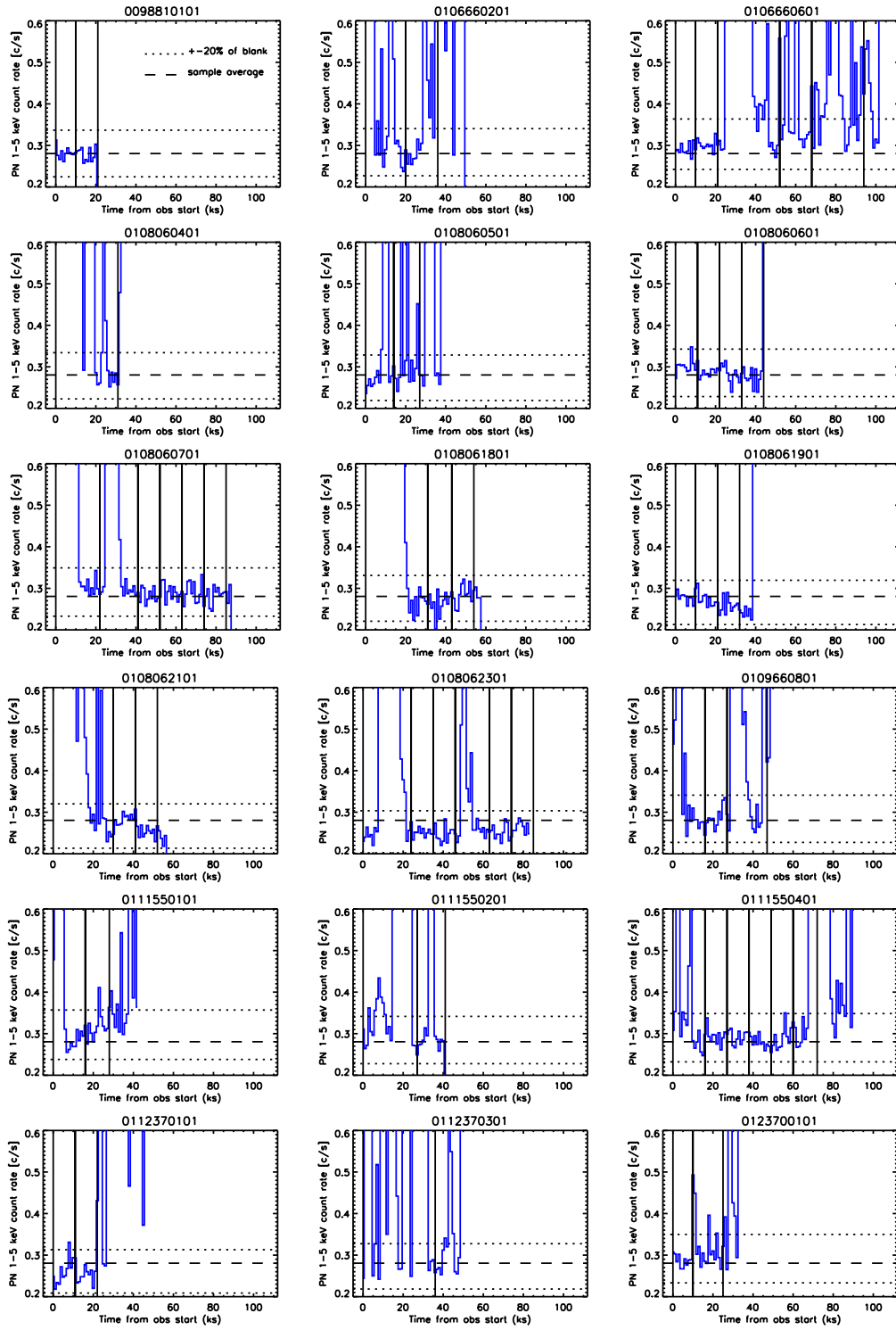


FIG. 8.— PN 1–5 keV light curves in 1 ks bins in the 12–15 arcmin annuli for the observations listed in Table 2, together with the sample-average quiescent rate (dashed line) and the $\pm 20\%$ limits around the individual mean (dotted line). The vertical lines show the start and stop times of the 10 ks periods used in the analysis.

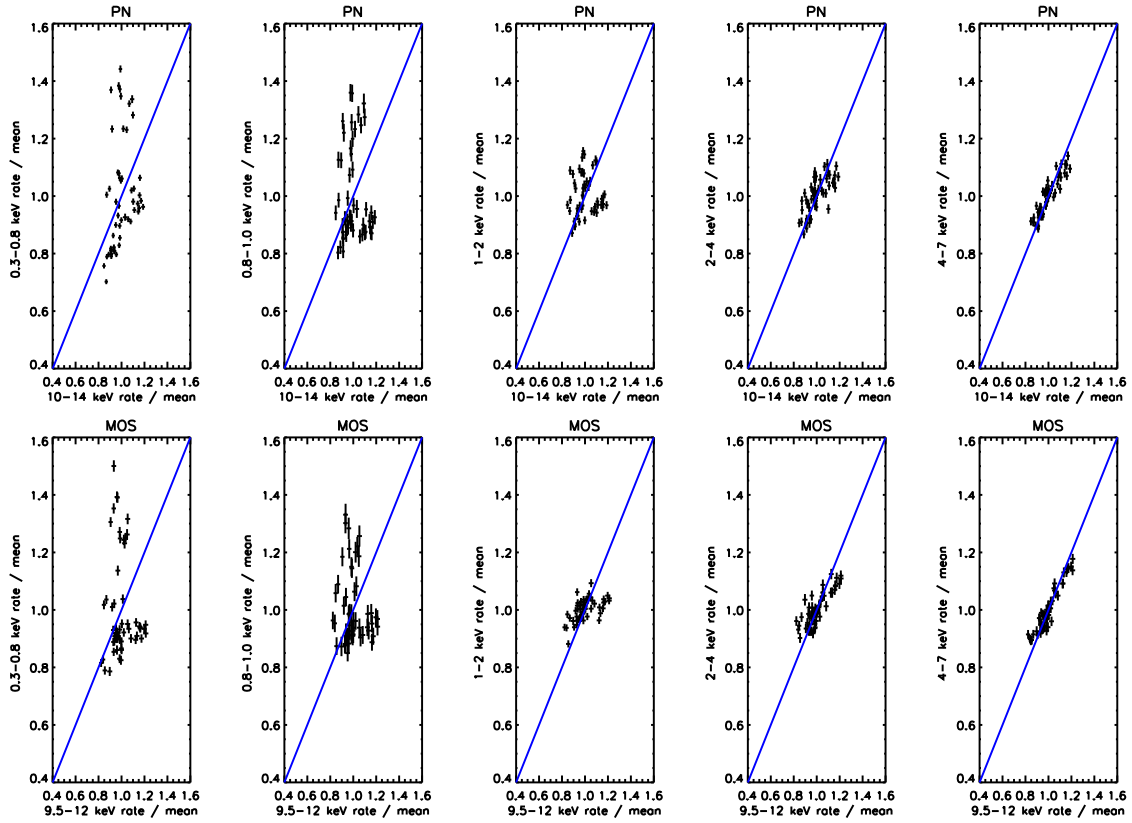


FIG. 9.— Quiescent double-filtered PN (upper row) and MOS (lower row) count rates, divided by the mean values, in the full FOV region for the 10 ks spectra sample, in 0.3–0.8–1–2–4–7 keV bins (columns) and in the hard band (10–14 keV for PN, 9.5–12 keV for MOS, rows) are shown by crosses. Uncertainties are statistical 1σ . The lines show predicted rates assuming that the individual count rates in the intervals of the 0.3–7 keV band deviate from the average by the same factor as in the hard band.

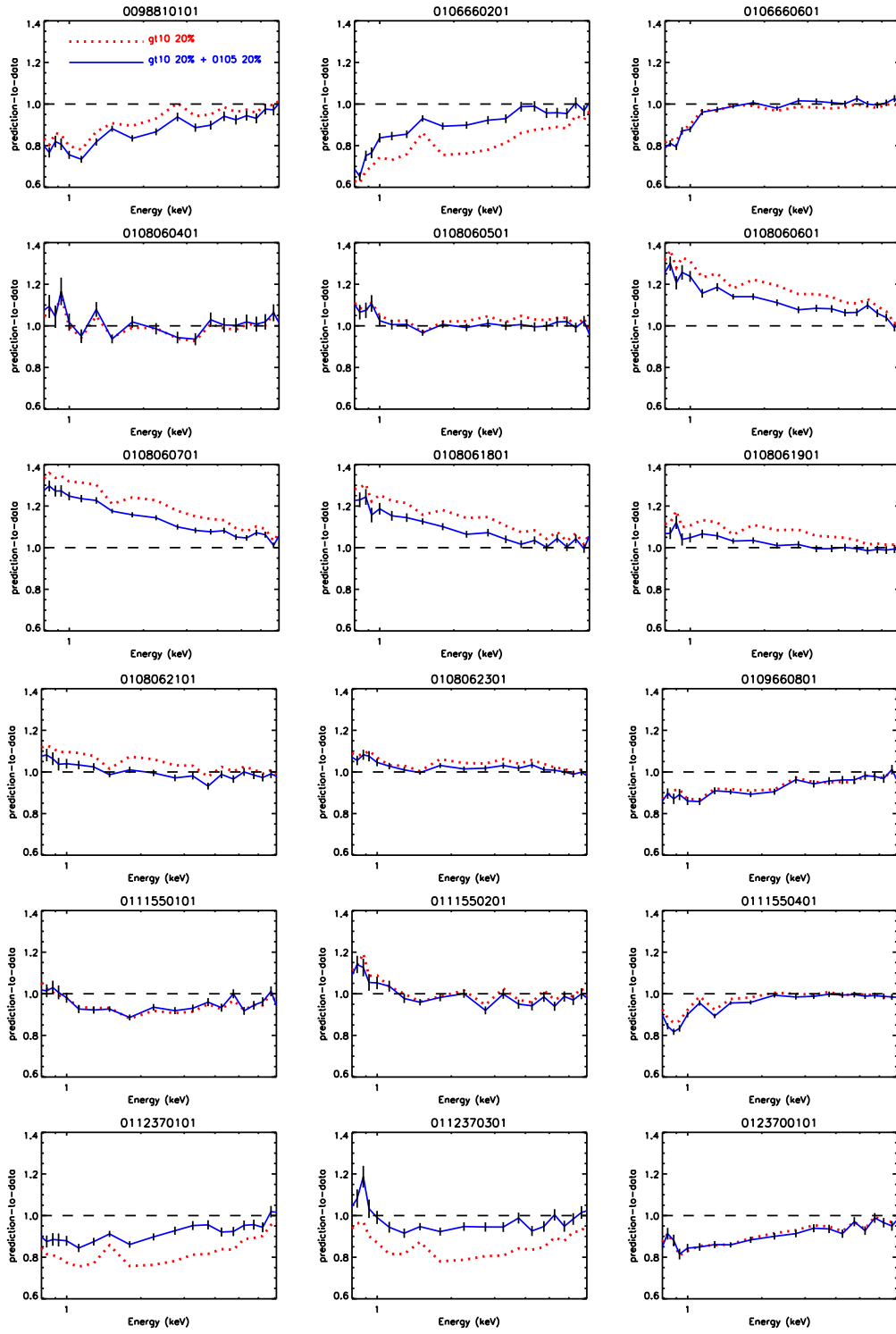


FIG. 10.— The ratio of the background prediction rates to the observed rates for each of the individual blank-sky pointings, using only the hard band filter (dotted line) or the double filter (solid line). The vertical bars on the solid lines show the statistical 1σ uncertainties

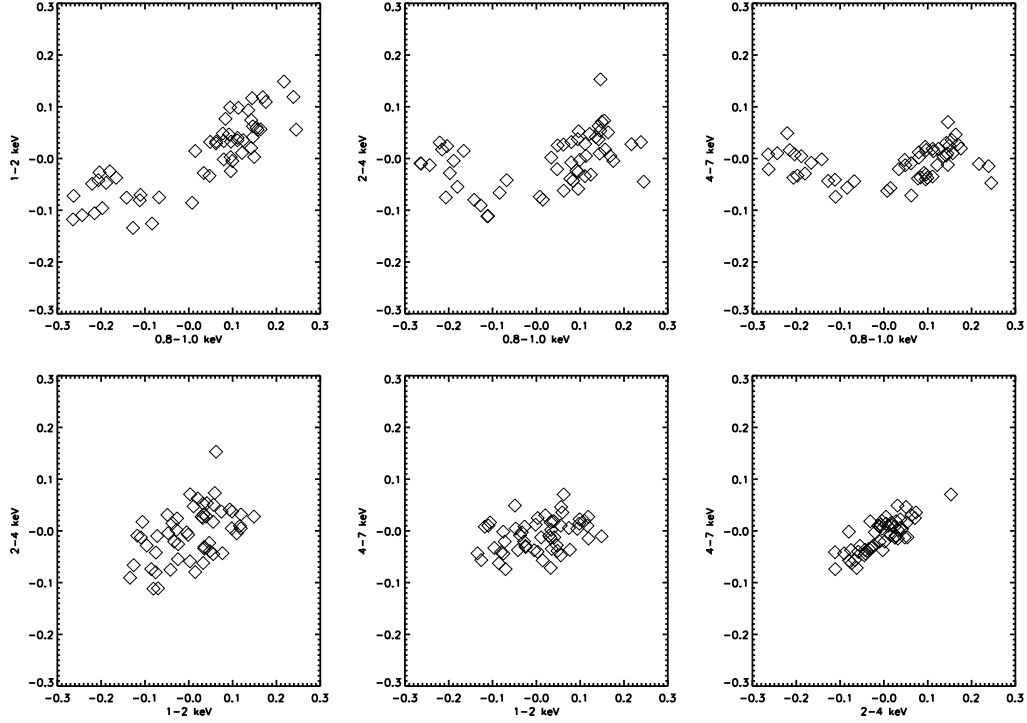


FIG. 11.— Relative deviations of the observed PN background from our predictions in different bands, (prediction - data)/data. The data are cleaned using the double-filter method and binned into 10 ks time bins.

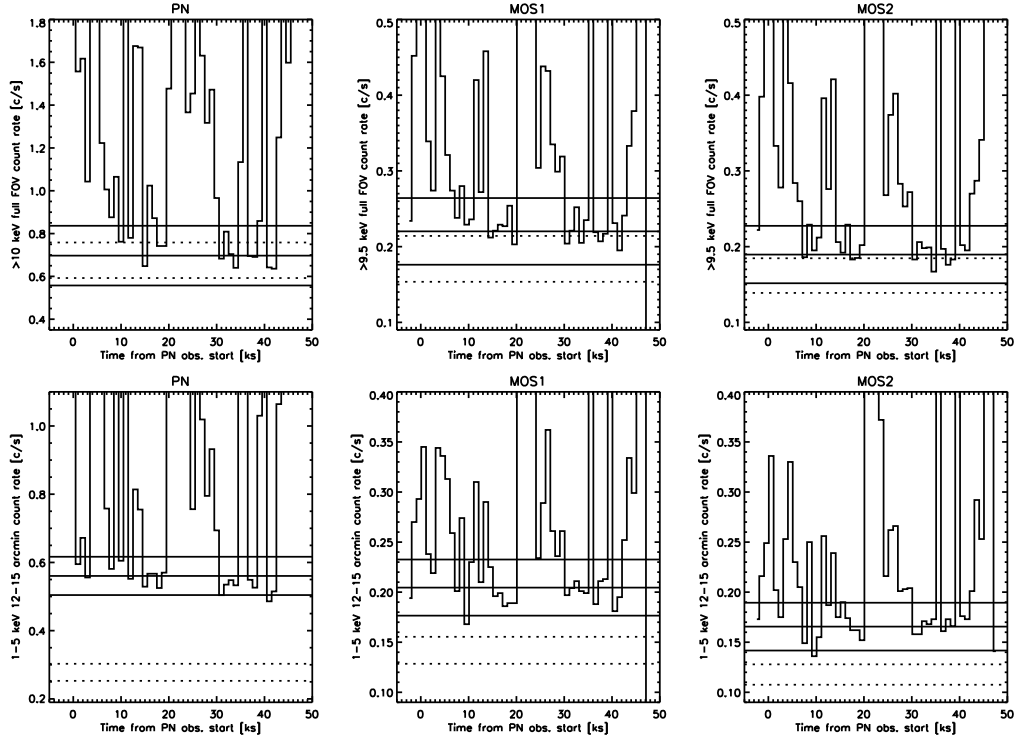


FIG. 12.— A1795 light curves (histograms) in the hard band for the full FOV (upper row) and in the 1–5 keV band for the 12–15 arcmin annulus (lower row), for PN (left column), MOS1 (middle column) and MOS2 (right column). The quiescence limits are shown with a solid line; the highest and the lowest of the individual blank-sky quiescence levels (see Table 3) are shown with dotted lines. The MOS2 blank-sky values are reduced by 15% due to the excluded peculiar CCD (see text).

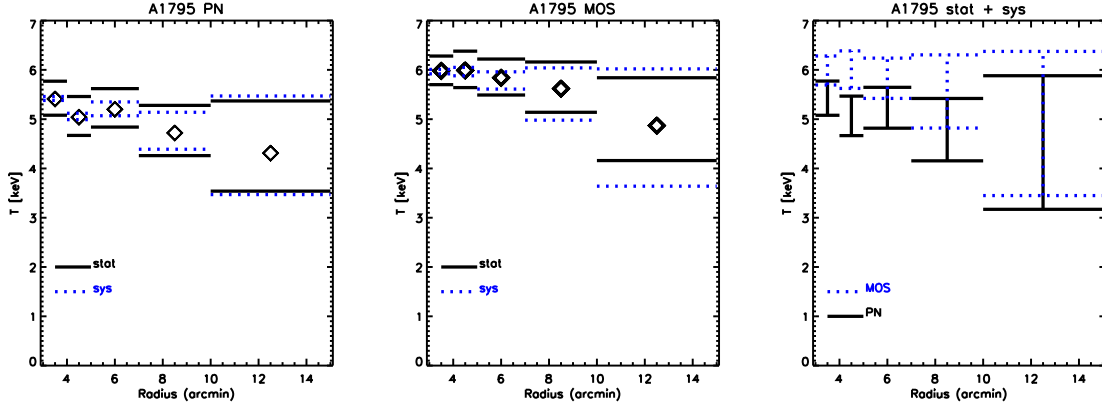


FIG. 13.— Best-fit temperatures (diamonds) of A1795 in the $r = 3-4-5-7-10-15'$ annuli for the double-filtered quiescent periods of PN (left panel) and MOS (middle panel), together with the statistical uncertainties (solid black lines, denoted as “stat”) and the background-induced systematic uncertainties using the exact error propagation method (§7.2.1, dotted blue lines, denoted as “sys”) at the 90% confidence level. Right panel shows the combined effect of the statistical and the background-induced systematic uncertainties (added in quadrature) on the temperature profile for PN (black solid line) and MOS (dotted blue line).

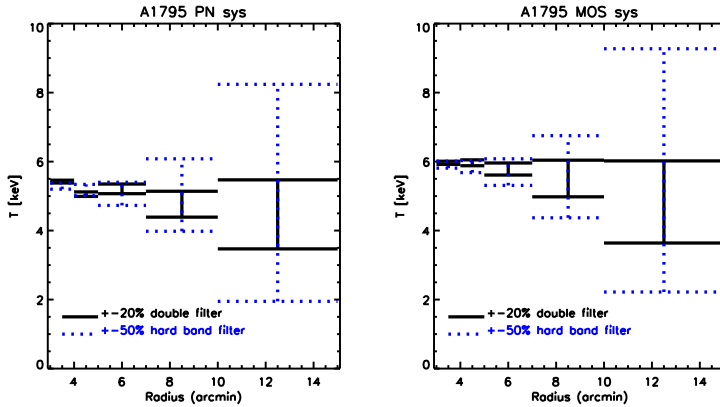


FIG. 14.— Background-induced systematic uncertainties using the exact error propagation method (§7.2.1) for the A1795 temperatures in our double-filtering method are shown by solid black line, while those in the less restrictive flare cleaning common in the literature (see text) by blue dotted line. PN is shown in left panel and MOS in right panel.